國立交通大學

機械工程學系

博 士 論 文

二維頻率偏移式微型加速度計結構設計

Structure Design of a 2D Frequency Shift Microaccelerometer

研 究 生：黃鐙輝

指導教授： 金甘平 博士

蕭國模 博士

徐文祥 博士

羅一中 博士

中 華 民 國 九 十 四 年 六 月

二維頻率偏移式微型加速度計結構設計

Structure Design of a 2D Frequency Shift Microaccelerometer

研 究 生：黃鐙輝　　Student：Deng-Huei Hwang

指導教授：金甘平，蕭國模　　Advisor：Kan-Ping Chin, Kuo-Mo Hsiao

徐文祥，羅一中　　Wensyang Hsu, Yi-Chung Lo

國 立 交 通 大 學

機械工程學系

博 士 論 文

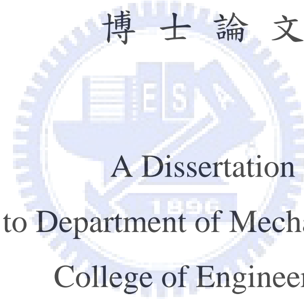

A Dissertation

Submitted to Department of Mechanical Engineering

College of Engineering

National Chiao Tung University

in Partial Fulfillment of the Requirements

for the Degree of

Doctor of Philosophy

in

Mechanical Engineering

June, 2005

Hsinchu, Taiwan, Republic of China

中華民國九十四年六月

國立交通大學

博碩士論文全文電子檔著作權授權書

(提供授權人裝訂於紙本論文書名頁之次頁用)

本授權書所授權之學位論文，為本人於國立交通大學機械工程系所 __固力控制__組， 93 學年度第__2__學期取得博士學位之論文。

論文題目：二維頻率偏移式微型加速度計結構設計
指導教授：金甘平、蕭國模、徐文祥、羅一中

■ 同意

本人茲將本著作，以非專屬、無償授權國立交通大學與台灣聯合大學系統圖書館：基於推動讀者間「資源共享、互惠合作」之理念，與回饋社會與學術研究之目的，國立交通大學及台灣聯合大學系統圖書館得不限地域、時間與次數，以紙本、光碟或數位化等各種方法收錄、重製與利用；於著作權法合理使用範圍內，讀者得進行線上檢索、閱覽、下載或列印。

論文全文上載網路公開之範圍及時間：

本校及台灣聯合大學系統區域網路	■ 中華民國 97 年 6 月 24 日公開
校外網際網路	■ 中華民國 97 年 6 月 24 日公開

■ 全文電子檔送交國家圖書館

授 權 人：黃鐙輝

親筆簽名：______________________

中華民國　　　年　　　月　　　日

國立交通大學

博碩士紙本論文著作權授權書

(提供授權人裝訂於全文電子檔授權書之次頁用)

本授權書所授權之學位論文，為本人於國立交通大學機械工程系所 __固力控制__組， 93 學年度第__2__學期取得博士學位之論文。

論文題目：二維頻率偏移式微型加速度計結構設計
指導教授：金甘平、蕭國模、徐文祥、羅一中

■ 同意

本人茲將本著作，以非專屬、無償授權國立交通大學，基於推動讀者間「資源共享、互惠合作」之理念，與回饋社會與學術研究之目的，國立交通大學圖書館得以紙本收錄、重製與利用；於著作權法合理使用範圍內，讀者得進行閱覽或列印。

本論文為本人向經濟部智慧局申請專利(未申請者本條款請不予理會)的附件之一，申請文號為：____________________________，請將論文延至_____年_____月_____日再公開。

授 權 人：黃鐙輝

親筆簽名：________________________________

中華民國　　　　年　　　　月　　　　日

file:////C|/Documents and Settings/HDH/桌面/Dissertation_Final/授權書_3pages_b.htm 第 2 頁 / 共 3 2005/6/24 上午 11:35:16

國家圖書館
博碩士論文電子檔案上網授權書

（提供授權人裝訂於紙本論文本校授權書之後）

ID:GT008414802

本授權書所授權之論文為授權人在國立交通大學機械工程系所 93 學年度第_2_學期取得博士學位之論文。

論文題目：二維頻率偏移式微型加速度計結構設計

指導教授：金甘平、蕭國模、徐文祥、羅一中

茲同意將授權人擁有著作權之上列論文全文（含摘要），非專屬、無償授權國家圖書館，不限地域、時間與次數，以微縮、光碟或其他各種數位化方式將上列論文重製，並得將數位化之上列論文及論文電子檔以上載網路方式，提供讀者基於個人非營利性質之線上檢索、閱覽、下載或列印。

※ 讀者基於非營利性質之線上檢索、閱覽、下載或列印上列論文，應依著作權法相關規定辦理。

授權人：黃鐙輝

親筆簽名：____________________

民國　　年　　月　　日

國 立 交 通 大 學

論 文 口 試 委 員 會 審 定 書

本校 機 械 工 程 學系博士班 黃 鐙 輝 君

所提論文(中文) 二維頻率偏移式微型加速度計結構設計

(英文) Structure Design of a 2D Frequency Shift Microaccelerometer

合於博士資格水準、業經本委員會評審認可。

口試委員：

指導教授：

系 主 任： 教授

中 華 民 國 九十四 年 六 月 十六 日

二維頻率偏移式微型加速度計結構設計

研究生：黃鐙輝

指導教授：金甘平 博士
蕭國模 博士
徐文祥 博士
羅一中 博士

國立交通大學機械工程學系

摘 要

此研究提出了一個雙軸加速度計，它具有以線性響應來反應所感測到之加速度，高抗擾動之結構剛性來減低發自垂直於感測方向之加速度或重力所造成的形變影響，結構對稱性以有效解耦平面加速度，以及對加速度具有高偵測靈敏度等優點。而它的設計考慮便是以頻率偏移原理，高深寬比結構設計，結構幾何對稱以及尺寸最佳化來達成上述的優點。另外，UV-LIGA 製程則被採用，藉以驗證此型結構的製作可行性。結果是，在所提出的振動式雙軸加速度計的模擬範例中，其響應之線性誤差小於 4%，因重力造成的結構變形小於 0.01 微米，跨軸靈敏度小於 0.002%，而感測靈敏度則可藉尺寸最佳化而被提升到 8%/G。此外，由於此結構優異的解耦特性，所推得的一維解析模型也可以用來推算受測的二維平面加速度。至於所採用的 UL-LIGA 製程則可製作出，深寬比大於 5，細長比大於 100，而絕對尺寸為 4×20×500 μm 的鎳材電鍍結構。由此等結果相較於早先提出的加速度計，可了解所提的振動式雙軸加速度計確實在性能上被顯著的提升，並且可以用簡單，經濟的製程來製作。

Structure Design of a 2D Frequency Shift Microaccelerometer

Advisors: Dr. Kan-Ping Chin
Dr. Kuo-Mo Hsiao
Student: Deng-Huei Hwang Dr. Wensyang Hsu
Dr. Yi-Chung Lo

Department of Mechanical Engineering
National Chiao Tung University

Abstract

This research proposes a structure of a 2D frequency shift microaccelerometer with good characteristics on linear response to respond the detected acceleration, high structure rigidity to resist influence from non-sensing axis acceleration, geometry symmetry to decouple a planar acceleration, and high sensitivity for sensing acceleration. In this design, the frequency shift principle, structure with symmetry geometry and also high-aspect ratio and the dimension optimization are adopted to fulfill the mentioned advantages. The results show that, the response linearity error for the simulated illustration is less than 4%, the deformation of the proof mass along gravitation direction is smaller than 0.01 μm, the cross-axis sensitivity is negligible less than 0.002%, and the sensitivity could be raised to 8%/G after dimension optimization. In addition, owing to the superior decoupling capability, the derived 1D analytical model can successfully calculate the sensed 2D planar acceleration. On the other side, the fabrication result of the adopted UV-LIGA process shows that, a 4 (w) × 20 (h) × 500 (l) μm nickel microbeam with high-aspect ratio 5 and slender ratio larger than 100 can be electroplated. In contrast to the previous design, the proposed 2D frequency shift microaccelerometer structure has a significant performance promotion and can be fabricated by using a simple and economic process.

Acknowledgements

這個加速度計畫緣起於服務於美國通用汽車公司張世佳博士在 1996 年回台時，跟我當時的指導教授金甘平老師以及羅一中老師提出的。很感謝金老師，羅老師還有張博士讓我有機會藉這個題目踏入微機電領域。金老師辭世後，有幸得到徐文祥老師的指導，讓我能夠完成論文投稿。經過徐老師的指點，不僅讓我學到如何清楚的鋪陳論述自己的研究成果，更讓我了解如何將研究工作做的踏實完整。還要再感謝徐老師的好脾氣包容我修改文章的疏漏。還有，對共同指導教授蕭國模老師對我的設想及勞心，在此我也要表示誠摯感謝。

金大仁老師，成維華老師，李安謙老師，白明憲老師，戈正銘老師，尹慶中老師等在課業上的啓蒙跟教導，學生在此致上最高的謝意。呂宗熙老師的指導跟包容我會永久感恩。

自從 1988 年進入機械系以來，幾乎接受過系上所有老師所開課程的啓發，機械系老師對學生總是傾囊相授，給學生機會也有期許。在此對我敬愛的老師們一併致謝。

還要感謝的是石修總經理讓我在 2000 年加入新磊的前身光磊微機電事業部，讓我有機會接觸建廠，制度建立，設備採購、安裝、維護，製程試作，元件研發，市場調查及應用開發等工作，讓我對微機電產業開了眼界。石修博士在待人處事上的指導也讓我受益匪淺。

此外，要感謝年近八十的雙親，姐姐、姐夫，還有老弟長久以來在精神及物質上的支持支援。去年內人淑媛的身體狀況確實讓我惶恐，希望她健康平安。三歲多的女兒羿文，感謝她讓我享有當父親的喜悅。

最後感謝所有相扶相助的貴人。

page

Abstract in Chinese ………………………………………………………………… i

Abstract …………………………………………………………………………ii

Acknowledgements ……………………………………………………………iii

Table of content …..…………………………………………………………..iv

List of Tables ……………………………………………………………………vii

List of Figures …….……… ……………………………………………………viii

Nomenclature ……………………………………………………………………xi

Chapter 1. Introduction ………………………………………………………… 1

1.1. Accelerometer Market and Applications ……………….…………… 3

1.2. General Performance Requirements …………………………………7

1.3. About Frequency Shift Principle ………………………………………..7

Chapter 2. Design Consideration ……………………………………………………...8

2.1. Consideration on Structure Rigidity ……………………………… 10

2.2. Consideration on Structure Symmetry ………………………………10

2.3. Consideration on Linear Response ……………………………………...10

2.4. Consideration on Sensitivity and Optimization ………………………10

Chapter 3. Design ……………………………………………………………...12

3.1. Literatures Review ……….…………………………………………12

3.2. Structure Design and Operation Principle ……………………………14

3.3. Analytical Model Derivation …………………………………………16

3.3.1. Analytical Model of the Microbeam ……………………………..16

3.3.2. Load Analysis of Microbeams …………………………………17

3.3.3. Buckling Analysis for Proof Mass ………………………………..19

3.3.4. Calculation of 2D Acceleration …………………………………...20

3.4. Analytical Simulation …………………………………………………21

page

3.5. Finite Element Analysis ……………………………………………..24

3.6. Performance Evaluation ……………………………………………..25

3.6.1. Linearity Evaluation …………………………………………….25

3.6.2. Deviation Evaluation of 1D analytical model to FEA …………..26

3.6.3. Decoupling Evaluation …………………………………………27

3.6.4. Cross-Axis Sensitivity Evaluation ………………………………27

3.6.5. Rigidity Evaluation ……………………………………………...28

3.7. Verification of Analytical Model with Experiment Data ……………29

3.8. Summary ……………………………………………………………..32

Chapter 4. Fabrication …………………………………………………………...33

4.1. Fabrication Consideration ……………………………………………33

4.2. Introduction of SU8-5 Photoresist ………………………………….....34

4.3. Experiment Equipment and Substrate …………………….................34

4.4. Fabrication Process …………………………………………………..35

4.5. Problem and Solution …………………………………………………...41

4.6. Fabrication Results ..…………………………………………………42

4.7. Summary ……………………………………………………………...47

Chapter 5. Optimization ……………………………………………………………48

5.1. Optimization and Sensitivity …………………………………………49

5.2. Dimension to be concerned for Sensitivity ……………………………50

5.3. Definition of Sensitivity Function ……………………………………50

5.3.1. Optimization of Structure Dimension …………………………….51

5.3.2. Structure Dimension Arrangement and Mechanical Sensitivity ….51

5.4. Optimization for Capacitor Dimension ………………………………..56

5.5. Summary ………………………………………………………………60

page

Chapter 6. Discussion …………………………………………………………..61

6.1. Modeling and Geometry ……………………………………………..61

6.2. Mechanical Sensitivity and Structural Dimension ….………………61

6.3. Fabrication ……………………………..……………………62

Chapter 7. Conclusion and Future works …………………………………………63

7.1. Conclusion for Design, Fabrication and Optimization ………………63

7.2. Future works ……………………………………………………………64

Reference ……………………………………………………………………..67

List of Tables

Table 1: General performance requirement for accelerometer …………………………..7

Table 2: Geometry parameters and mechanical properties in simulations …………..22

Table 3: Symbol used in the simulation results ……………………………………...23

Table 4: Analytical and FEA simulation conditions ………………………………...23

Table 5: Experimental data in reference [5] …………………………………………31

Table 6: Performance comparison between DFSM design [5] and the current design ……………………………………………………………………………..32

List of Figures

Figure 1. Accelerometer market shares estimation ……………………………......4

Figure 2. Market shares estimation for accelerometer used for measurement and control ………………………………………………………………………..4

Figure 3. Global accelerometer market …………………………………………....5

Figure 4. Application principle of MEMS accelerometer …………………………6

Figure 5. The structure of the 2D HAR resonant microbeam microaccelerometer ..9

Figure 6. The exggeratedly deformation tendency of the microbeams due to a Y-directional acceleration …………………………………………………………15

Figure 7. The primary vibration mode of the clamped-clamped microbeam B subject to an axial load ……………………………………………………………………15

Figure 8. The boundary of microbeam C comprising a fixed clamped end and a movable clamped end [21] ……………………………………………………..15

Figure 9. Fig. 5. Free body diagram of the proof mass M under acceleration a, subject to axial forces T_A and T_B from the microbeams A and B, and two reactions P, respectively, from the beams C and D ……………………………………………19

Figure 10. Buckling of the clamped-clamped microbeam B subject to the axial load T_B under the maximum acceleration …………………………………………………20

Figure 11. The exaggeratedly deformation tendency of the microbeams under a planar acceleration a ……………………………………………………………………20

Figure 12. The characteristic dimension of the accelerometer; the thickness of the proof mass and that of the microbeam are identical, indicated by h as shown in Figure 5(b) ……………………………………………………………………………21

Figure 13. The frequency shift of the microbeam of the proposed accelerometer at F1-8 condition ……………………………………………………………………22

Figure 14. The frequency shift difference between the analytical model and FEA at F1-8 and F2-8 conditions ………………………………………………………….23

Figure 15. Linearity error of the shifted natural frequency ………………………..26

Figure 16. The deviation of the 1D model related to FEA. ………………………..26

Figure 17. The little deviation between the analytical simulation and FEA indicates the good decoupling capability …………………………………………………….27

Figure 18. The largest cross-axis sensitivity between X and Y directions is less than 0.002% ………………………………………………………………………………..28

Figure 19. The FEA simulation shows the maximum Z-directional displacement of the proof mass under 1G is about 0.507×10^{-9} m ………………………………………28

Figure 20. Change's dual-axis natural frequency-shifted microaccelerometer (DFSM) [5] ……………………………………………………………………………………..30

Figure 21. Frequency evaluation of the DFSM [5] using the derived model, the sensitivity is 160 Hz/G ………………………………………………………………..31

Figure 22. Steps for processing SU8-5 ……………………………………………35

Figure 23. Spin speed and film thickness …………………………………………37

Figure 24. Soft bake time and film thickness ……………………………………...38

Figure 25. Exposure time and film thickness ……………………………………...39

Figure 26. PEB time and film thickness ……………………………………………40

Figure 27. Development time and film thickness …………………………………..41

Figure 28. Gap is misshaped due to the snaking structure. The original gap dimension on the SU8-5 mold, is 16 μm width × 1000 μm long × 55 μm deep ……43

Figure 29. The dimension of gap on the SU8-5 mold, is 18 μm width× 1000 μm long × 55 μm deep ……………………………………………………………………….43

Figure 30. Stain appeared in trench …………………………………………………43

Figure 31. The bottom of the SU8-5 structure is encroached by the developer 44

Figure 32. The encroached structure is disappeared using proper exposure recipe ...44

Figure 33. 2D microaccelerometer structure made of Ni using electroplating 45

Figure 34. The close-up view of the structure shown in Figure 33 46

Figure 35. Close up view of the microbeam, electrode pad and their sidewalls. The dimension of the microbeam is about 4×20×500 μm 46

Figure 36. The sensitivity evaluation of microaccelerometers with thickness *h* of 20 μm, confined by *W*=*L*+*2l*=6000 μm 52

Figure 37. The distribution of the vertical displacement of proof mass due to Z-directional gravitation or acceleration 54

Figure 38. The maximum detectable acceleration for the illustrated microaccelerometers 55

Figure 39. The dimension of the separation *v* is to be optimized to maximize the capacitance change ratio for the capacitor under a voltage application 55

Figure 40. Dimension optimization for separation *v* 58

Figure 41. The change ratio of the capacitance *S*(*v*) of the capacitor of the microaccelerometer under the application of a voltage at 10V. The length *l* of the microbeam is 1500μm, the separation *v* and gap *d* are respectively ranged from 0.1 *l* to 0.5 *l* and 2 to 7 μm 58

Figure 42. The estimation of original capacitance Co 65

Figure 43. Schematic diagram of driving, sensing circuits and PLL 66

Nomenclature

A : cross sectional area of microbeam

A_c : the area of capacitor plate

a : acceleration

a_n : eigenvalue of nth normal mode shape function

a_x : X-directional component of the planar acceleration

a_y : Y-directional component of the planar acceleration

b_n : eigenvalue of nth normal mode shape function

C_0 :original capacitance

C :capacitance

C_1, C_2, C_3 and C_4: constant coefficients of first normal mode shape function

E : Young's modulus

f_e: Electro static force

$f(G,L,l,w)$: Shifted natural frequency of microbeam due to acceleration;

f_o and $f_o(L,l,w)$: Natural frequency of microbeam;

Δf, $\Delta f(G)$ and $\Delta f(G,L,l,w)$: frequency difference between $f(G,L,l,w)$ and $f_o(L,l,w)$;

h : thickness of microbeams and proof mass

I : area moment of inertia

L : width of the square proof mass

l : length of microbeam

M : mass magnitude of proof mass

M_o : moment applied upon beam's tip

m : mass per unit length of microbeam

P : concentrated force applied upon the tip of the microbeam; reaction appeared on the tips of microbeams C and D, applying to the proof mass

q_e : electrostatic force per unit length,

$S(L,l,w)$: Sensitivity function of microaccelerometer;

$S(v)$: change ratio of capacitance

T : axial force applied to microbeam

T_A : axial reaction applied to proof mass by the elongated microbeam A

T_B : axial reaction applied to proof mass by the compressed microbeam B

T : axial force applied to microbeam

T_{max}: The maximum axil loading befor buckling

T_{crx}: The critical axil loading of buckling

t : time

V : volume of proof mass

V :voltage

W : width of the microaccelerometer anchor frame

ε_0 : the permittivity constant

v : separations for separating the electrode pad from the proof mass, and from the anchor.

w : width of microbeams

x : distance along the length of the microbeam

y : transverse deflection of the microbeam

δ : resultant deflection of the microbeam

ρ : volumetric mass density

φ_n : n^{th} normal mode shape function

ω_n : n[th] natural frequency

Chapter 1
Introduction

Since the successful achievement from MEMS technology which has been developed for more than twenty years, the silicon based microaccelerometer featured in low cost, small size, reliable and easy use is able to meet the requirement of the current application market. Though, the request of quality and quantity to microaccelerometer is continually increased during the expansion of application market, the price is strongly depressed, however, the performance is requested to promote. Thus, the capability to meet the change of the performance requirement from single sensing axis and low resolution to two or three sensing axes but high resolution, MEMS accelerometer with relative lower cost but higher performance is always being considered as a candidate to replace the conventional accelerometer with higher precision. The application evolution of the microaccelerometer is started from replacing the conventional accelerometer used in airbag for automobile ten more years ago, then extended to automotive body altitude monitor, operation and control safety couple years ago, and right now a new application opportunity is appeared for the tiny sensor to work with the information technology (IT) product. The actual application for IT product includes attitude or tilt sensing, movement detection and civil guidance and navigation accompanying with GPS. The attitude and tilt sensing application is prosperously growing in recent year due to the numerous video projector requested by the developing home entertainment market. To improve the image quality, accelerometer is installed in the projector to detect the body attitude and tilt angle to correct the image keystone to compensate and modify the distorted projection image.

To exceed the performance of the proof-mass-displacement type MEMS accelerometer adopted by the attitude and tilt application, a frequency-shift type

accelerometer is proposed here. The precision property of the conventional quartz based accelerometer is well known, however, due to the benefits of low cost, volume production and size miniaturization, a MEMS silicon vibrating accelerometer is prospected to replace the conventional one. In fact, the vibrating microaccelerometer has been proposed since the beginning of '90, and new design is always proposed by every year. However, the majority of the proposed sensors are the one-axis accelerometer, and the minority two-axis accelerometer is always suffered from the poor rigidity of the structure resulting from the cumbersome conventional MEMS process. Hence, to improve the drawback for the old two-axis vibrating accelerometer, present research proposes a structure of a 2D frequency shift microaccelerometer with good characteristics on linear response, high structure rigidity to resist influence from non-sensing axis acceleration, geometry symmetry to decouple a planar acceleration, and high sensitivity. In the design consideration, the frequency shift principle, the high-aspect ratio structure with symmetry geometry and the dimension optimization are adopted to fulfill the mentioned advantages. The results show that, the response linearity error for the simulated illustration is less than 4%, the deformation of the proof mass along gravitation direction is smaller than 0.01 μm, the cross-axis sensitivity is negligible less than 0.002%, and the sensitivity could be raised to 8%/G after dimension optimization. In addition, owing to the superior decoupling capability, the derived 1D analytical model is able to calculate the sensed 2D planar acceleration. On the other side, the result of the adopted UV-LIGA process shows that, a 4 (w) × 20 (h) × 500 (l) μm nickel microbeam with high-aspect ratio 5 and slender ratio larger than 100 is electroplated. In contrast to the previous design, the proposed 2D frequency shift microaccelerometer structure has a significant performance promotion and can be fabricated by using a simple and economic process.

1.1. Accelerometer Market and Applications

According to the forecast of Nexus and Yole [1], MEMS accelerometer market will be $600 million in 2005. Figure 1 shows that, $510 million about 85% of the market is about the application of movement monitoring and event detection, and the other $90 million about 15% is for measurement and control [2].

As shown in Figure 2, for the market of measurement and control, the accelerometers has to meet the precision requirement in application such as, defense IMU (Inertial Measurement Unit), tilt detection and stabilization, civilian guidance, aeronautics, seismic detection and instrumentation.

Figure 3 shows that, the market of movement monitoring and event detection includes the applications for hard disk drive, transportation data logging, airbag in automobile, patient activity, machining monitoring, and pacemakers. The cost for accelerometer employed for this application category is about $1 to $50 per unit, and the performance of offset stability to working range is ranged from 10 to 0.1%. On the other side, the market of measurement and control includes the applications of civil IMU, plateform stabilization, seismic detection, instrumentation and robotics, compress and tilt detection, aeronautics, and defense IMU. The accelerometer for this kind of precise application is cost from $20 to more than $1000 per unit, and the offset stability to working range ratio is ranged between 0.1 to 0.001%.

To implement the low cost MEMS accelerometer used by the application of movement monitoring and event detection in Figure 3, the physical principles shown in Figure 4, such as piezoresistive, piezoelectric, surface-micromachining capacitive, thermal and optical are adopted.

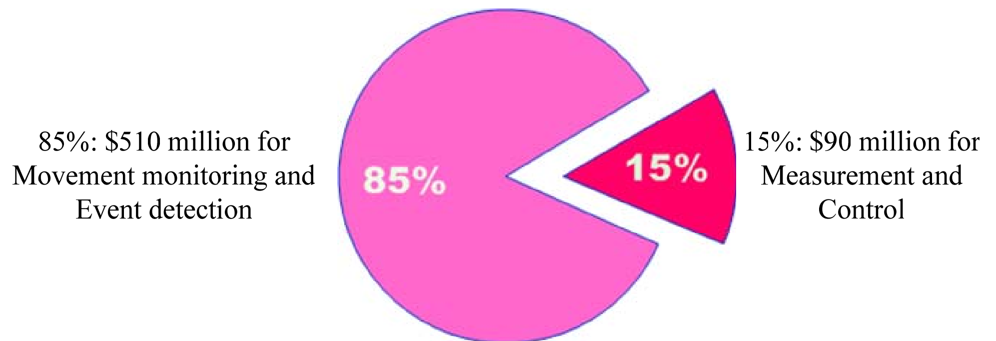

Figure 1. Accelerometer market shares estimation

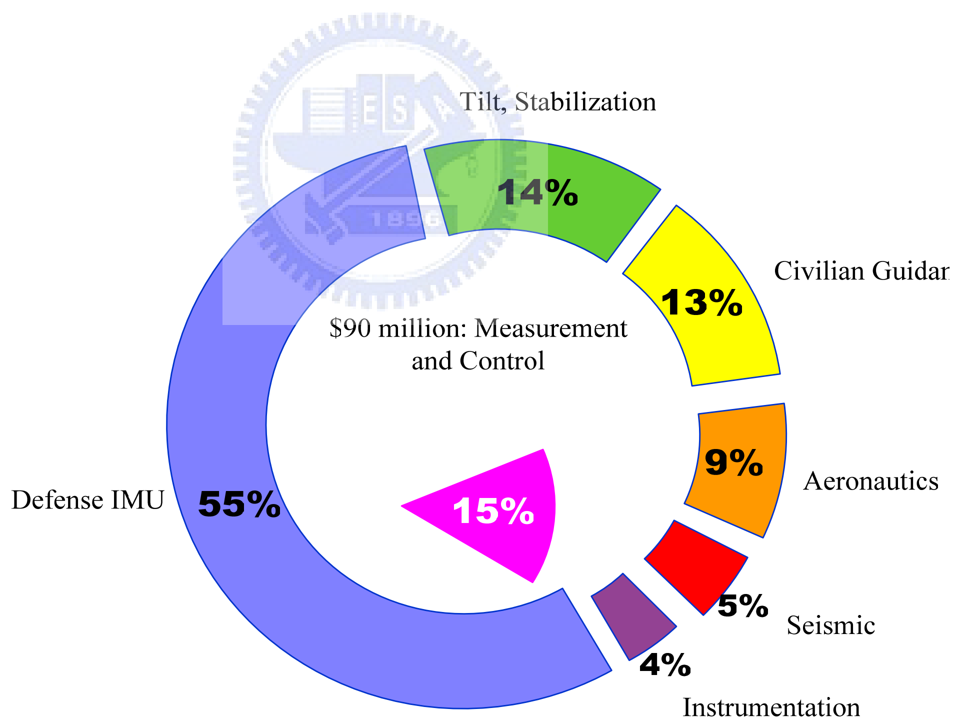

Figure 2. Market shares estimation for accelerometer used for measurement and control.

As to the measurement and control application, the high end MEMS accelerometer using bulk-micromachining capacitive or surface-micromachining capacitive principle is employed. However, to meet the requirement of precision application of aeronautics and defense IMU, the accelerometer operating in vibration principle, made by micro-mechanical machining, such as laser machining is the preferred choice.

At present time the mechanical machining quartz-based vibrating accelerometer is adopted for precision measurement, however, due to high quality and high profitable, MEMS vibrating accelerometer is being developed and used to supplant the conventional quartz-based accelerometer.

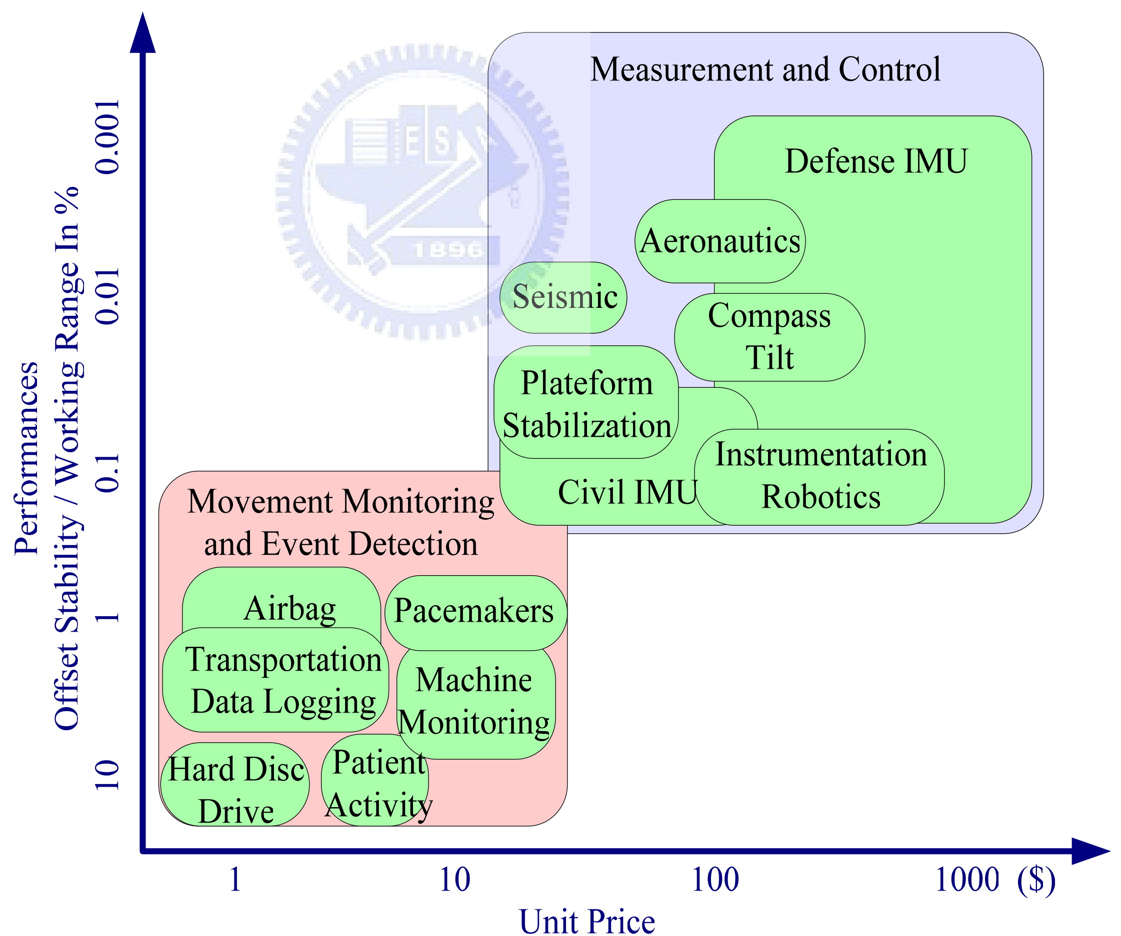

Figure 3. Global accelerometer market

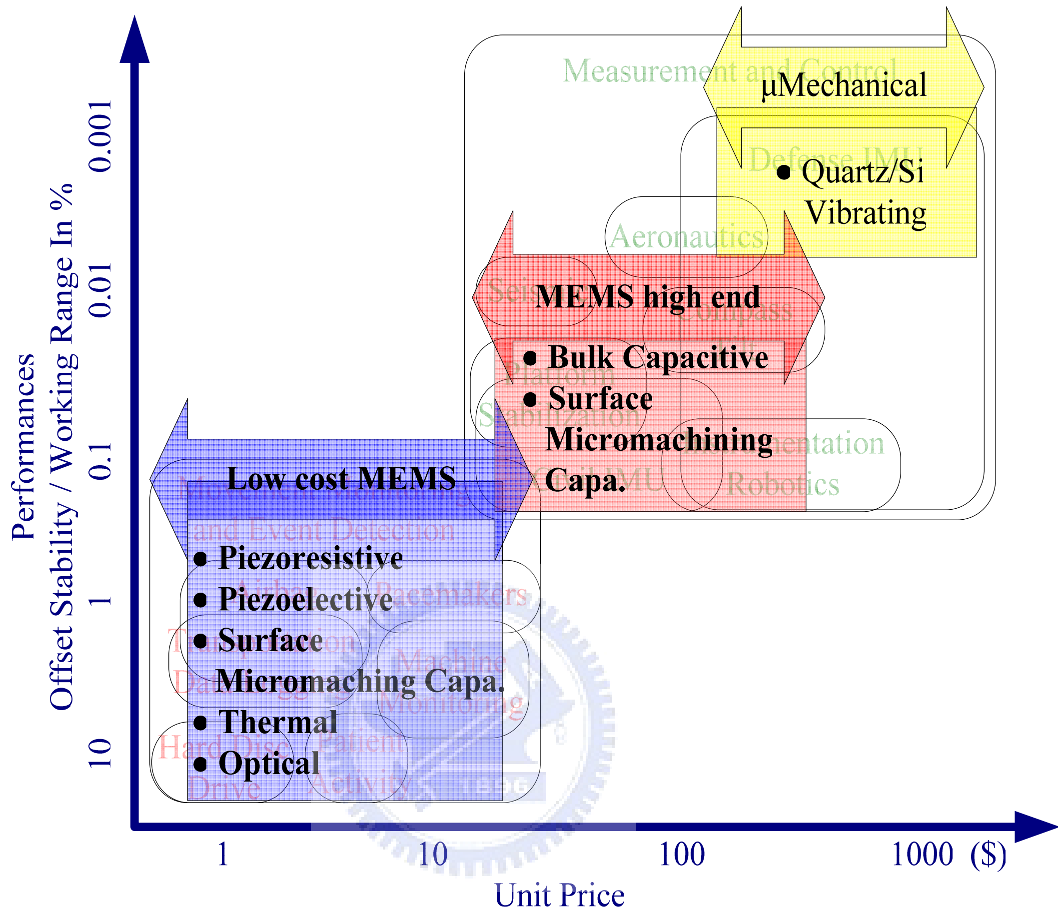

Figure 4. Application principle of MEMS accelerometer

1.2.General Performance Requirements

Table 1: General performance requirement for accelerometer

Parameter	Definition/Description	Physical Quantity
Offset (Bias)	The measurement of its average output when a specified g force is applied.	V, Hz
Offset hysteresis	Offset variation after a specified application.	V, Hz
Sensitivity (Gain)	The average gain over a force range.	V/g, Hz/g
Linearity error (FS)	How closely the sensitivity over the force range approximates a straight line.	%
Transverse sensitivity Cross-Axis Sensitivity	A measurement of what percentage of a force applied perpendicular to the sensitive axis of the device.	% of on-axis output
-3dB frequency	Bandwidth	Hz

Courtesy of NeoStone MicroFabrication Corporation.

The general performance requirement for an accelerometer is listed in Table 1.

1.3. About Frequency Shift Principle

The natural frequency of a mass-spring vibration system is determined by $\omega = (k/m)^{1/2}$. Thus, if an external or environmental application such as force, acceleration can change the system parameters k or m [3], the natural frequency ω of the mass-spring system can be shifted responding to this external application, then if a relation between the external application and the natural frequency can be established, the external application can be measured by evaluating the shifted natural frequency. In addition, the frequency shift principle is attractive in performing precision measurement, due to its characteristics on linear response, intrinsic sensitivity and quasi-digital signal output.

Chapter 2

Design Consideration

The previous researches [3~8] show that, the important factors considered for designing structure of the microaccelerometer include response behavior, structure geometry, structural rigidity and dimension arrangement. The response behaviors mean that a linear dynamic response is preferred for its easiness to be processed, and a nature of significant variation tendency responding to the detected acceleration is the other requirement. In addition, a symmetrical geometry configuration is necessary to decouple a detected 2D acceleration into two independent acceleration components. The structure having the rigidity and stiffness is necessary to reduce the deformation or dynamic influence due to other non-interested acceleration or gravitation. More, the dimensions of the structural components dominate the mechanical and electrical sensitivity of the device.

In this research, these factors are considered to meet the general performance requirement listed in Table 1. That is, the requirements about offset and its hysteresis, linearity error, cross-axis sensitivity and sensitivity are met by the design consideration on rigidity, linear response, decoupling capability and dimension optimization, respectively.

According to the factors, a 2D frequency shift microaccelerometer used for attitude and tilt sensing in a constant acceleration or gravitation filed is proposed, as shown in Figure 5. This accelerometer is configured with a central proof mass connected via four identical and symmetrical microbeams with high-aspect-ratio. This accelerometer is intended to operate by using electrostatic force and sense the acceleration by using natural frequency shift of the microbeam. Thus, on the two sidewalls of each microbeam two electrode pads Gd and Gs are respectively disposed to form the

capacitors for driving and sensing the transverse vibration of the microbeam. When the microaccelerometer shown in Figure 5 is accelerated to right, the inertial effect of the proof mass *M* applies compression and tension respectively on the microbeams C and the D, and thereby shifts their natural frequencies. The electrode pad Gd generates a variable electrostatic force to actuate the microbeam D to vibrate at its shifted natural frequency and the vibrating frequency of the excited microbeam D is detected by the electrode pad Gs.

2.1. Consideration on Structure Rigidity

To meet the offset and offset hysteresis requirements, structural rigidity is necessary to against deformation due to gravitation, which is fulfilled by structure with high-aspect-ratio in the proposed design. The high-aspect-ratio characterization makes the microbeam itself is capable of reducing the deflection due to the connected proof mass under gravitation or acceleration perpendicular to the planar acceleration. The high-aspect-ratio characterization also provides the degree of freedom for the capacitor disposed on the sidewall of the microbeam to be expanded by employing UV-LIGA process to build up the microstructure [9, 10].

2.2. Consideration on Linear Response

The principle of the natural frequency shift of the microbeam is adopted by the microaccelerometer to measure acceleration to meet the linearity error requirement. The merits of using natural frequency as an output signal are, on theoretically it has high sensitivity and linearly frequency shift in response to a measured physical or chemical signal, and on practically it posses a quasi-digital nature as being adopted to be an output signal, that making the resonant type sensor itself easy to be integrated into a digital system [3].

2.3. Consideration on Structure Symmetry

To reduce the cross-axis sensitivity, the symmetric structure is chosen to decouple a planar acceleration into two independent accelerations, which induces little crosstalk. In addition, due to its compact and simple configuration, the response of 2D microaccelerometer in sensing acceleration can be described easily and precisely by the concise analytical model without complicated calculation.

2.4. Consideration on Sensitivity and Optimization

To obtain a most sensitive microaccelerometer structure, the relationship between the detecting sensitivity and the dimension for the proof mass and the microbeam has to be realized [11]. To investigate the variation of sensitivity related to the variation of geometry dimension, the microaccelerometers with different dimensions confined within the constraint of $W=L+2l$ are considered. In Figure 5, L is the width of the proof mass and l represents the length of the microbeam.

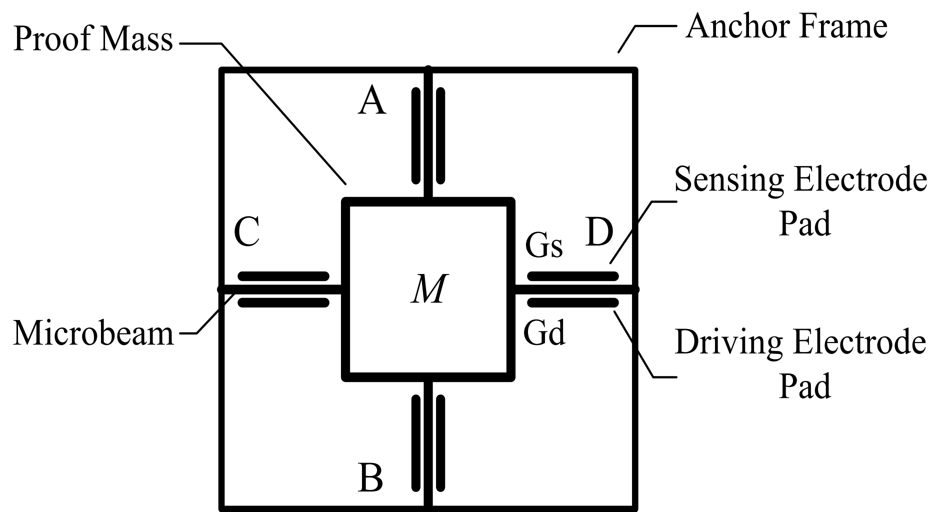

Figure 5 (a). Top view.

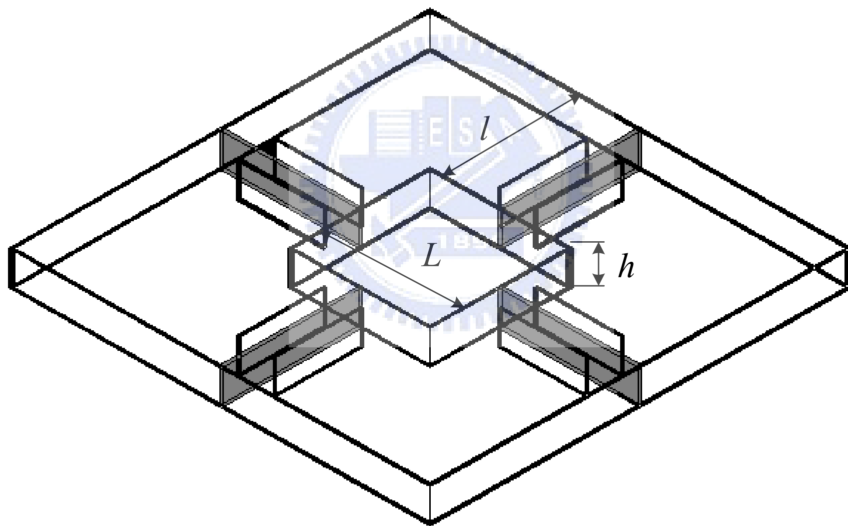

Figure 5 (b). Elevation view

Figure 5. The structure of the 2D HAR resonant microbeam microaccelerometer

Chapter 3
Design

An accelerometer with concise structure having resonant microbeam to measure 2D acceleration is proposed. This structure is configured with a central proof mass suspended by four symmetrical and orthogonal high-aspect-ratio (HAR) microbeams. This dual-axis design is able to decouple a two-axis signal from a 2D acceleration. An analytical model relating the linear relationship between the acceleration and the associated resonant frequency shift of microbeam is derived, and a finite element analysis (FEA) is also performed to confirm this model. The FEA result also shows that there is little cross talk between X and Y directions measurement, meaning that this structure is able to decouple a planar 2D acceleration into two independent acceleration components, and therefore the 1D analytical model can be used to evaluate the 2D acceleration on the X-Y plane. In addition, the model is verified by the testing results of one conventional dual-axis natural frequency shifted microaccelerometer (DFSM) [5]. The simulation result also shows that the sensitivity of the proposed HAR accelerometer is triple over that of the conventional DFSM.

3.1. Literatures Review

Due to the remarkable sensitivity and linear response, many micro sensors based on frequency shift principle have been developed, including micro accelerometers [4~7, 12~16]. In which, the resonant frequency of the accelerometer structure or its substructure e.g. vibrating beam will be shifted by the variations of structure strain, stress [4~7, 12~14], or rigidity [15, 16]. However, most of the previous micro accelerometers using frequency shift principle were only capable of measuring 1D acceleration, except Chang's design [5], a dual-axis natural frequency shifted

microaccelerometer (DFSM), which could successfully decouple a two-axis signal and detect a 2D acceleration. However, the rigidity of its microbridge fabricated by the surface micromachining was too weak to resist deflection caused by the connected proof mass, and thus additional constraint bridges were required to support the proof mass, leading to a complex structure, which not only complicated the model derivation and fabrication process, but also reduced the acceleration measurement sensitivity. Besides, due to the inherent limitation resulting from the surface micromachining, the available area underneath the microbridge for forming capacitors to respectively drive and detect vibration was difficult to enlarge.

Here a HAR (high-aspect-ratio) resonant microbeam accelerometer to detect a planar 2D acceleration is proposed, which can be fabricated by various novel micromachining techniques, such as DRIE [17], LIGA [18] and LIGA-like process [9, 11, 19]. In contrast to the conventional DFSM design [5], the proposed accelerometer is configured with a suspending proof mass supported by just four identical, orthogonal, and HAR microbeams, requiring no constraint bridges, since the HAR feature can enhance rigidity along the gravitational direction to support the proof mass without sacrificing the structural compliance in plane. In addition, comparing to the limited capacitor area formed underneath the supporting microbridges in conventional DFSM, the capacitors in the proposed design are placed at two sides of microbeams, then the area of the capacitors can be enlarged by HAR structure. Also, a thicker and heavier proof mass can be obtained without using the complex leverage mechanism [4, 12, 13] to increase sensitivity.

An analytical model is first derived here to relate the natural frequency shift of microbeam and the applied acceleration by following the classic mechanics and vibration theory [20, 21]. Finite Element Analysis (FEA) and experimental data from previous literature [5] will also be used to confirm the analytical model and show the

sensitivity improvement of the proposed design.

3.2. Structure Design and Operation Principle

The structure of the proposed high-aspect-ratio dual-axis frequency shift microaccelerometer is shown in Figure 5 Fig. 1. This microaccelerometer is operated using electrostatic force, and two respective electrode pads Gd and Gs adjacent to the two side walls of each microbeam are placed to form two capacitors to drive and sense the transverse vibration of the microbeams A, B, C and D. To distinguish the term of "microbridge" in conventional DFSM design [5], "microbeam" is adopted here to describe the HAR beam in current design with larger thickness.

Figure 6 shows the microaccelerometer under acceleration along Y direction, the inertial effect of the proof mass *M* applies a tensile and a compression on the microbeams A and the B, respectively, which will shift the natural frequencies of this two microbeams, as shown in Figure 7. To detect such Y-directional acceleration, the driving electrode pads Gd shown in Figure 5 generate the variable electrostatic forces to respectively actuate the microbeams A and B to vibrate at their natural frequencies. On the other side, the sensing electrode pads Gs respectively sense the natural frequency variations of the excited microbeams A and B. Thus, if a relationship between the acceleration and the shifted natural frequency of the microbeam subject to the axial load is realized, the Y-directional acceleration can be evaluated by the natural frequency shift. Similarly, the X-directional acceleration can also be evaluated by the same way using microbeams C and D.

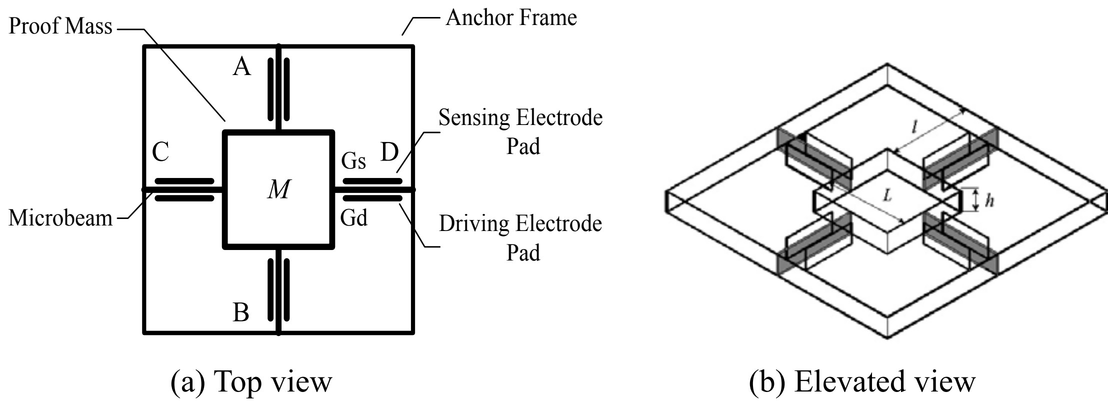

(a) Top view (b) Elevated view

Figure 5. The proposed HAR 2D resonant microbeam accelerometer. (Repeat)

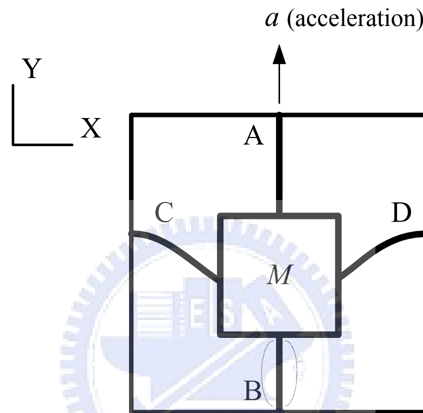

Figure 6. The exggeratedly deformation tendency of the microbeams due to a Y-directional acceleration.

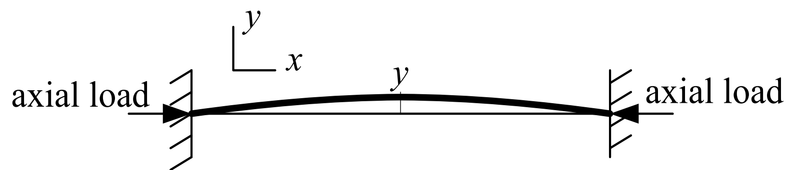

Figure 7. The primary vibration mode of the clamped-clamped microbeam B subject to an axial load.

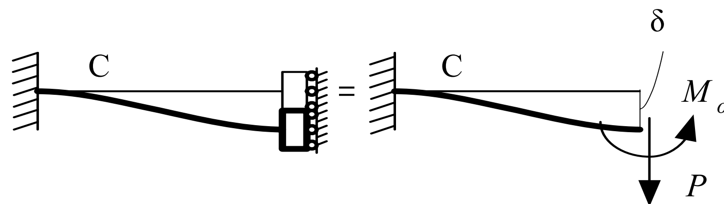

Figure 8. The boundary of microbeam C comprising a fixed clamped end and a movable clamped end [21].

3.3. Analytical Model Derivation

Here a model based on Euler-Bernoulli beam theory is derived to estimate the natural frequency shift of the microbeam. Comparing to the proof mass, the inertial effect of the microbeam is negligible, and thus is ignored in this derivation.

3.3.1. Analytical Model of the Microbeam

To estimate the frequency shift of the microbeams A, B, C, and D, as shown in Figures 5 and 7, the continuous system theory in [20] depicting the transverse vibration of elastic beam subject to an axial force T, with a clamped-clamped boundary condition, are used.

The governing equation is

$$EI\frac{\partial^4 y}{\partial x^4}+T\frac{\partial^2 y}{\partial x^2}+\rho A\frac{\partial^2 y}{\partial t^2}=0 \tag{1}$$

The clamped-clamped boundary condition is expressed as

$$y(x,t)|_{x=0}=0, \qquad \frac{\partial y(x,t)}{\partial x}|_{x=0}=0;$$

$$y(x,t)|_{x=l}=0, \qquad \frac{\partial y(x,t)}{\partial x}|_{x=l}=0.$$

To evaluate the fundamental natural frequency of the microbeam, the assumed mode method is used to solve Eq. (1). The 1st mode shape function of the microbeam is derived and shown as

$$\phi_1=C_1\cosh(a_n x)+C_2\sinh(a_n x)+C_3\cos(b_n x)+C_4\sin(b_n x) \tag{2}$$

where

$$a_n=\left[\frac{1}{2}\left(-\frac{Tl^2}{EI}+\sqrt{\left(\frac{Tl^2}{EI}\right)^2+\frac{4m\omega_n{}^2 l^4}{EI}}\right)\right]^{\frac{1}{2}} \tag{3}$$

$$b_n = \left[\frac{1}{2} \left(\frac{Tl^2}{EI} + \sqrt{\left(\frac{Tl^2}{EI} \right)^2 + \frac{4m\omega_n^{\ 2} l^4}{EI}} \right) \right]^{\frac{1}{2}} \tag{4}$$

and $m = \rho A$.

By substituting the clamped-clamped boundary condition into Eq. (2) to solve the undetermined constant coefficients C_1, C_2, C_3, and C_4, the characteristic equation can be obtained as

$$\left(a_n^{\ 2} - b_n^{\ 2}\right)\sinh(a_n)\sin(b_n) + 2a_n b_n \left[1 - \cosh(a_n)\cos(b_n)\right] = 0 \tag{5}$$

From Eq. (5), the shifted natural frequency of microbeam subject to an axial load T can be calculated. However, when the axial load on the microbeam is zero, the fundamental natural frequency of the microbeam becomes

$$\omega_1 = 22.4\sqrt{\frac{EI}{ml^4}} \tag{6}$$

3.3.2. Load Analysis of Microbeams

The boundary constraints of each microbeam A, B, C or D, can be considered as one end fixed on the anchor frame, and the other one is clamped on the movable proof mass accelerated along the Y-direction, as shown in Figure 8 Fig. 4, by taking microbeam C as an example. It can be seen that the deflection on the movable clamped end of microbeam C is caused by a concentrated force P and a moment M_o at the end due to the proof mass under acceleration. Thus, the resultant deflection of the microbeam C due to the assumed concentrated force P together with the moment loading M_o is

$$\delta = \frac{Pl^3}{12EI} \tag{7}$$

Based on the structural continuity, the bending deflections of the microbeams C and D, as shown in Figure 8, must equal to the elongation of the microbeam A and the shrinkage of the microbeam B, respectively, due to the axial tension T_A and the compression T_B. Therefore,

$$\delta = \frac{T_A l}{EA} = -\frac{T_B l}{EA} \tag{8}$$

As shown in Figure 9, in equilibrium, the forces P, T_A, and T_B exerted on the proof mass M under acceleration a, must satisfy following relation

$$T_A + T_B + 2P - Ma = 0 \tag{9}$$

Combine Eqs. (7), (8), and (9), the relation between the P, T_A, and T_B of each microbeam in terms of acceleration can be obtained.

$$P = \frac{6MaI}{Al^2 + 12I} \tag{10}$$

$$T_A = -T_B = Ma\left(\frac{1}{2} - \frac{6I}{Al^2 + 12I}\right) \tag{11}$$

When the axial loads in Eq. (11) due to 1D acceleration is substituted into Eqs. (3), (4), and (5), the corresponding natural frequency shift for the stressed microbeams can be calculated. Thereby, the relationship between acceleration and shifted natural

frequency is established.

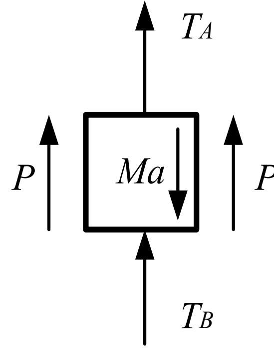

Figure 9. Fig. 5. Free body diagram of the proof mass M under acceleration a, subject to axial forces T_A and T_B from the microbeams A and B, and two reactions P, respectively, from the beams C and D.

3.3.3. Buckling Analysis for Proof Mass

When a microbeam is buckled due to the axial compression, its vibration frequency is zero, from Eqs. (3)-(5). Thus, a buckling analysis is necessary to determine the maximum measurable acceleration for the compressed clamped-clamped microbeam. The allowable maximum axial compression $T_{B\max}$ occurred on microbeam B, as shown in Figure 10, has to be less than the ultimate buckling load [22], i.e.

$$T_{B\max} \le T_{cr} = \frac{4\pi^2 EI}{l^2} \tag{12}$$

To determine the proof mass dimension, the bulking load limitation of Eqs. (11) and (12) are used. It is found that

$$T_{B\max} \cong \frac{M}{2} a_{\max} \tag{13}$$

Thus, from Eqs. (12) and (13), the width L of proof mass M can be determined by specifying the length l of the microbeam and the maximum detectable acceleration a_{max}.

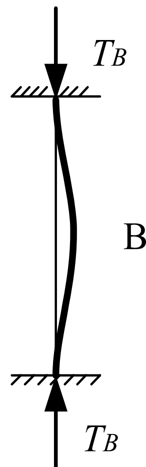

Figure 10. Buckling of the clamped-clamped microbeam B subject to the axial load T_B under the maximum acceleration.

3.3.4. Calculation of 2D Acceleration

If the proposed structure design can decouple the signals from two axes coupled 2D acceleration, the 1D analytical model can be used to estimate a planar 2D acceleration shown in Figure 11. Use Eqs. (11), (3), (4), and (5) to calculate the shifted natural frequencies for the microbeams A, B, C, and D under axial loads, the X and Y acceleration components a_x and a_y can be evaluated respectively, and then the vector sum of these two components represents the planar acceleration a.

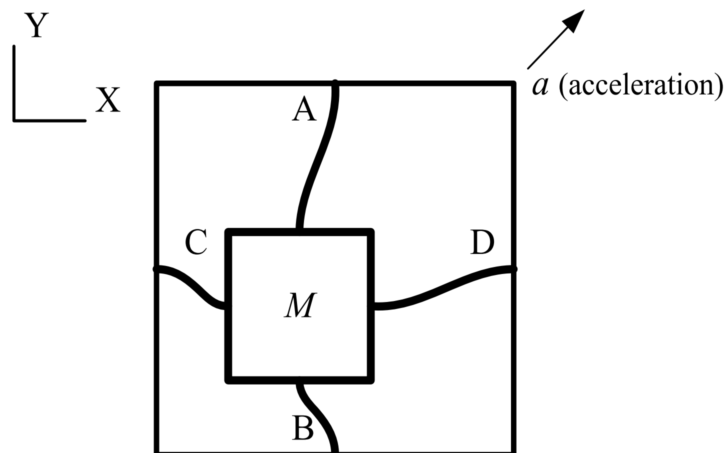

Figure 11. The exaggeratedly deformation tendency of the microbeams under a planar acceleration a.

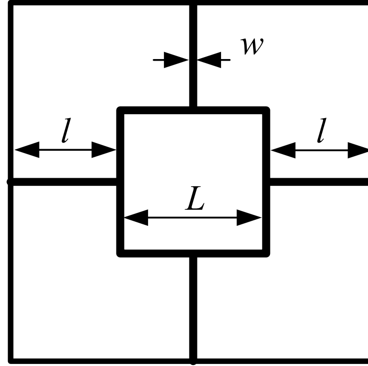

Figure 12. The characteristic dimension of the accelerometer; the thickness of the proof mass and that of the microbeam are identical, indicated by h as shown in Figure 5(b).

3.4. Analytical Simulation

The material properties of nickel and the geometry parameters of the microaccelerometer listed in Table 2 are used for analytical and FEA simulation. Figure 12 shows the characteristic dimension L is the width of the square proof mass, while l and w are the length and the width of the microbeam, respectively. The analytical simulation results are shown in Figure 13, and the symbols Ta, Ca, Da, Tf, Cf and Df are explained in Table 3, in which, the capital letter T and C respectively represent the frequency shift due to tension and compression, and D is the frequency difference between these two frequency shifts, while the index a and f represent the result from analytical simulation and finite element analysis, respectively. The conditions for analytical or FEA simulations are listed Table 4.

Table 2: Table 1: Geometry parameters and mechanical properties in simulations

Dimension and Property \ Material	Ni
Length of the microbeam l (μm)	1000
Width of the microBeam w (μm)	5
Thickness of the Beam and the Proof Mass h (μm)	20
1st mode natural frequency f_o (KHz) of the clamped-clamped microbeam	25.107
The assigned Maximum Detectable Acceleration (G)	10
Young's Modules E (Gpa)	210
Mass Density ρ(Kg/m^3)	8800
Mass of the Proof Mass M (Kg)	3.521×10^{-5}
Width of the Proof Mass L (μm)	14144.9

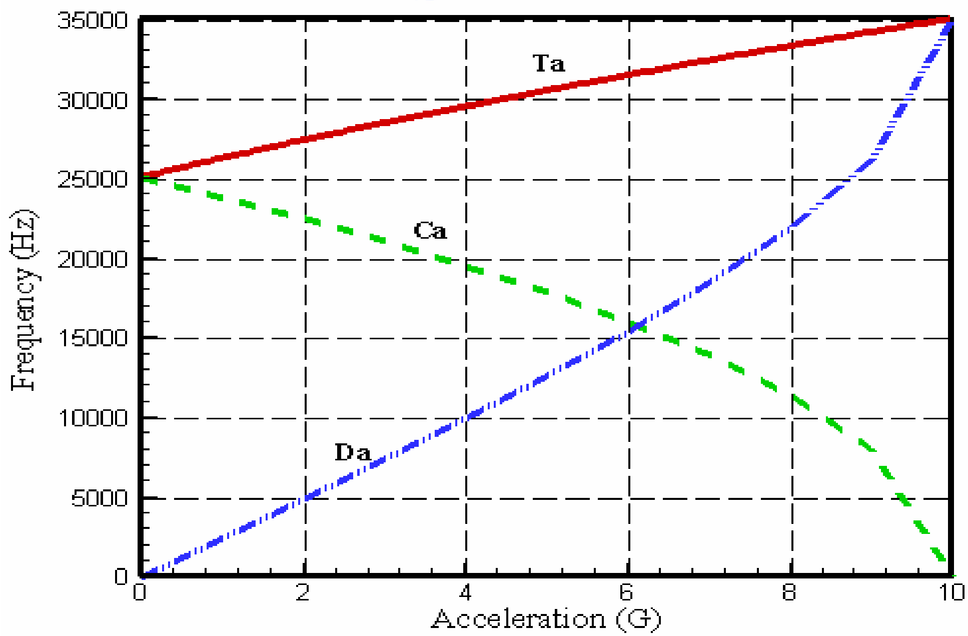

Figure 13. The frequency shift of the microbeam of the proposed accelerometer at F1-8 condition.

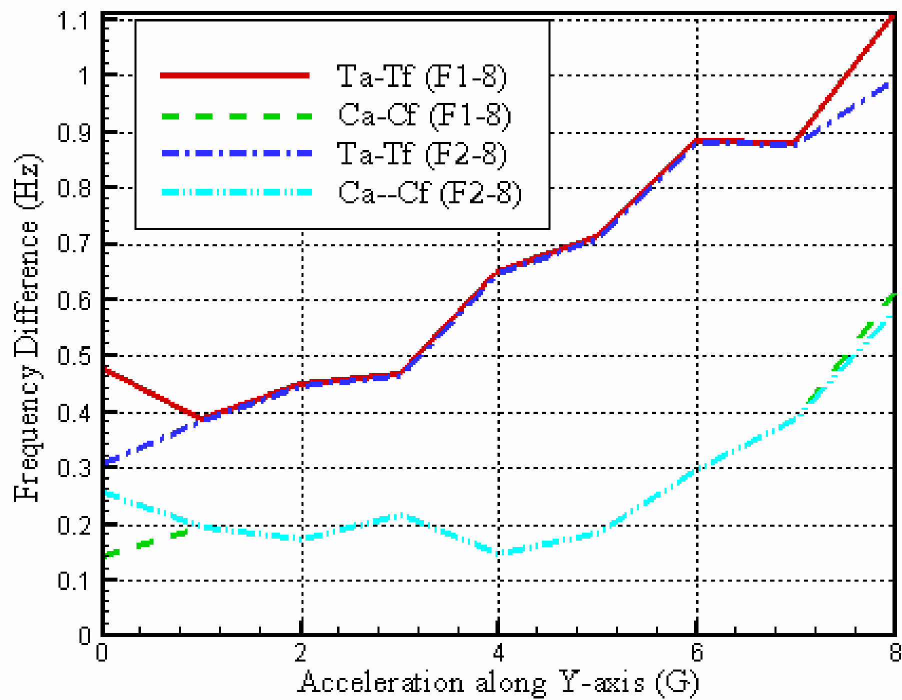

Figure 14. The frequency shift difference between the analytical model and FEA at F1-8 and F2-8 conditions.

Table 3: Symbol used in the simulation results

Simulation Object:	Symbol for Analytical Simulation	Symbols for FEA Simulation
Natural Frequency Shift Due to Tension	Ta	Tf
Natural Frequency Shift Due to Compression	Ca	Cf
Difference of Two above Natural Frequencies Shifts	Da = Ta-Ca	Df = Tf-Cf

Table 4: Analytical and FEA simulation conditions

Simulation Conditions	Direction / Acc. Dim.	X Direction (G)	Y direction (G)		
			Start	End	Inc
F1-8	1D Acceleration	0	0	8	1
F2-8	2D Acceleration	8	0	8	1

Figure 13 shows that the natural frequency shifts of microbeams under tension and compression are all quite linear with respect to the applied accelerations below 8 G, and the detecting sensitivity of Da is about 2,400 Hz/G. By buckling analysis, the microbeam subject to axial compression buckles at 10 G, and the corresponding resonant frequency becomes zero, thereby the difference of the frequency shift increases abruptly at 10 G.

3.5. Finite Element Analysis

To realize the dynamic effect of the suspended proof mass, the inertia effect of the microbeam, and the structural cross talk, which are ignored in the analytical model, the FEA software ANSYS® is employed to verify the analytical results. FEA elements shell 63 and beam 4 are respectively adopted to depict the behaviors of the proof mass in acceleration detecting and the microbeams in natural frequency shifting, respectively. The imposed boundary condition on the position of the microbeam connected to the anchor frame is clamped and stationary. Whereas, the boundary condition on the other end of the microbeam connected to the proof mass is a movable clamped end, and only translations along X, Y and Z directions are allowed. Through static and prestressed modal analysis of FEA, the natural frequency shift of the microbeam responding to the acceleration is obtained.

In Table 4, the condition F1-8 means an external 1D acceleration from 0 to 8 G in Y direction with an increment of 1 G in simulations, and the case F2-8 means an external 2D acceleration comprised by a Y-directional acceleration changing from 0 G to 8 G by an increment of 1 G in Y-direction and a constant acceleration of 8 G in X direction. To verify the capability of the structure to decouple a planar 2D acceleration into two independent components a_x and a_y, and validate the 1D analytical model to evaluate the acceleration components, both analytical model and FEA simulations are

performed for cases F1-8 and F2-8.

The deviation of simulation results between analytical model and FEA are shown in Figure 14. The solid line Ta-Tf (F1-8) in Figure 14 is less than 1.1 Hz indicating that the mass of microbeam ignored in analytical model causes little deviation to FEA result, on the other side, the dash-dot line Ta-Tf (F2-8) is less than 1 Hz, means that there is little deviation when using the 1D derived model to do a 2D simulation, lines Ca-Cf (F1-8) and Ca-Cf (F2-8) also have the same results. In addition, the maximum shrinkage of microbeam with length of 1000 μm before buckling is less than 0.007 μm, as shown in Figure 14. It indicates that not only the cross talk of the proposed microaccelerometer is very small and negligible, but also the assumption of clamped-clamped boundary condition in the analytical model has very little influences on the simulation result. The result verifies that the derived 1D analytical model is able to estimate two independent acceleration components of a 2D acceleration, decoupled by the proposed structure.

3.6. Performance Evaluation

The considered design factors i.e. linearity, rigidity, decoupling capability and sensitivity, which are achieved by frequency shift principle, high-aspect ratio structure, structure symmetry and dimension optimization. The results below show the coincidence between of the considered factors and the performance of the proposed 2D mcroaccelerometer structure.

3.6.1. Linearity Evaluation

The linearity error of the frequency output shown in Figure 15 is less than 4% for the natural frequency shifted due to tension or compression only, and is less than 7% for the difference between the shifted frequency due to tension and compression.

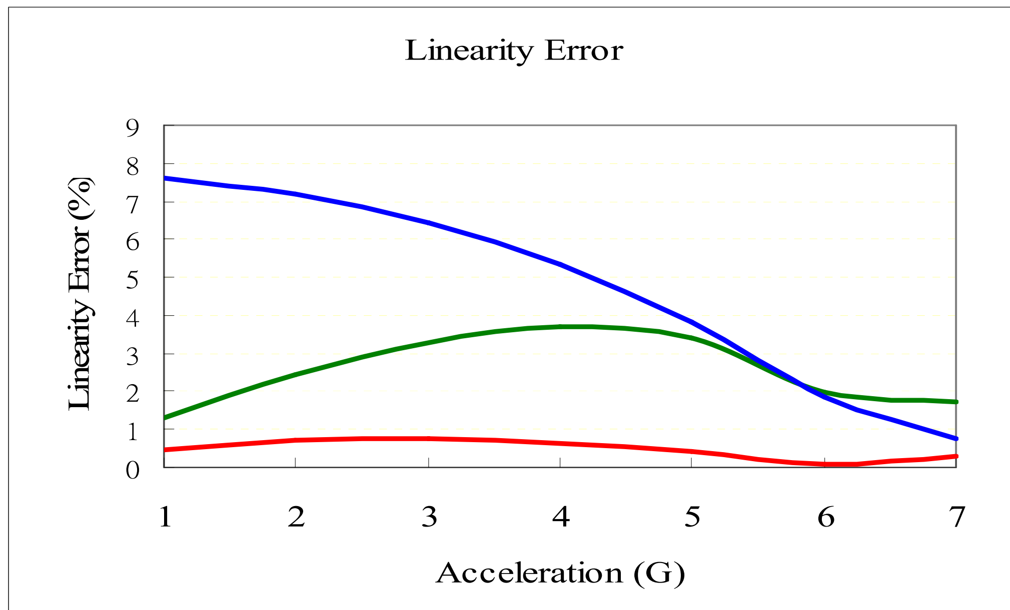

Figure 15. Linearity error of the shifted natural frequency.

3.6.2. Deviation Evaluation of 1D analytical model to FEA

The simulation results in Figure 16 shows that, the absolute deviation between the derived model and FEA is less than 0.6 Hz, and the corresponding relative one is less than 0.008%. That validates the exactness of the derived model.

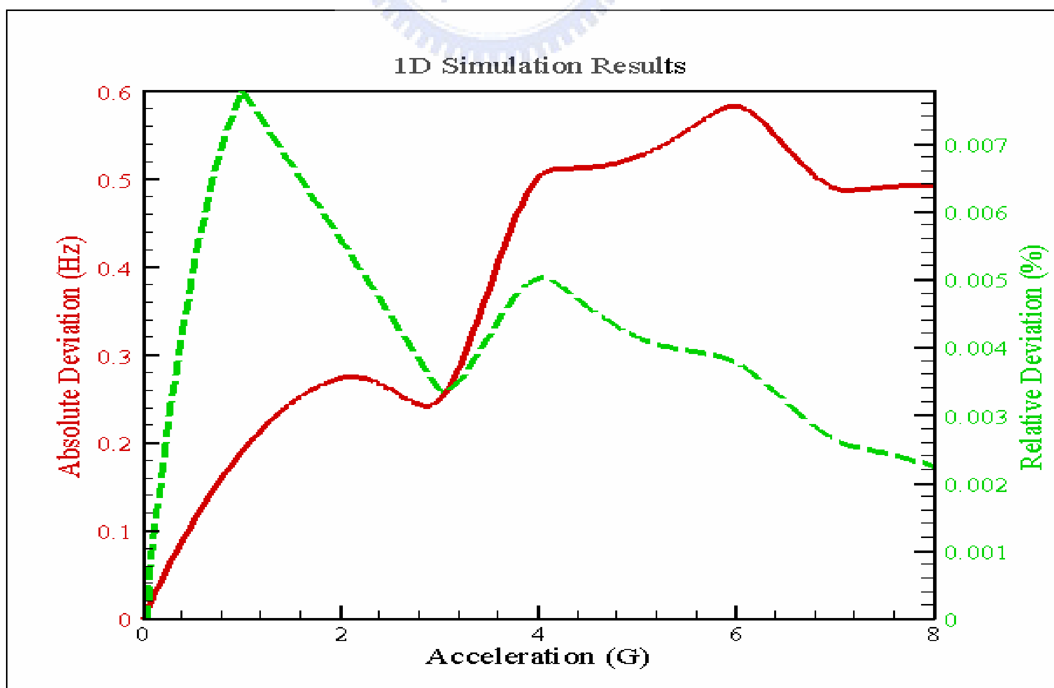

Figure 16. The deviation of the 1D model related to FEA.

3.6.3. Decoupling Evaluation

The FEA results in Figure 17 show the absolute and relative deviation between the 2D FEA and analytical simulation is less than 0.6 Hz and 0.0078%, it means that the symmetric structure is able to decouple the planar acceleration into two independent components, and the derived model can be used to evaluate the planar acceleration.

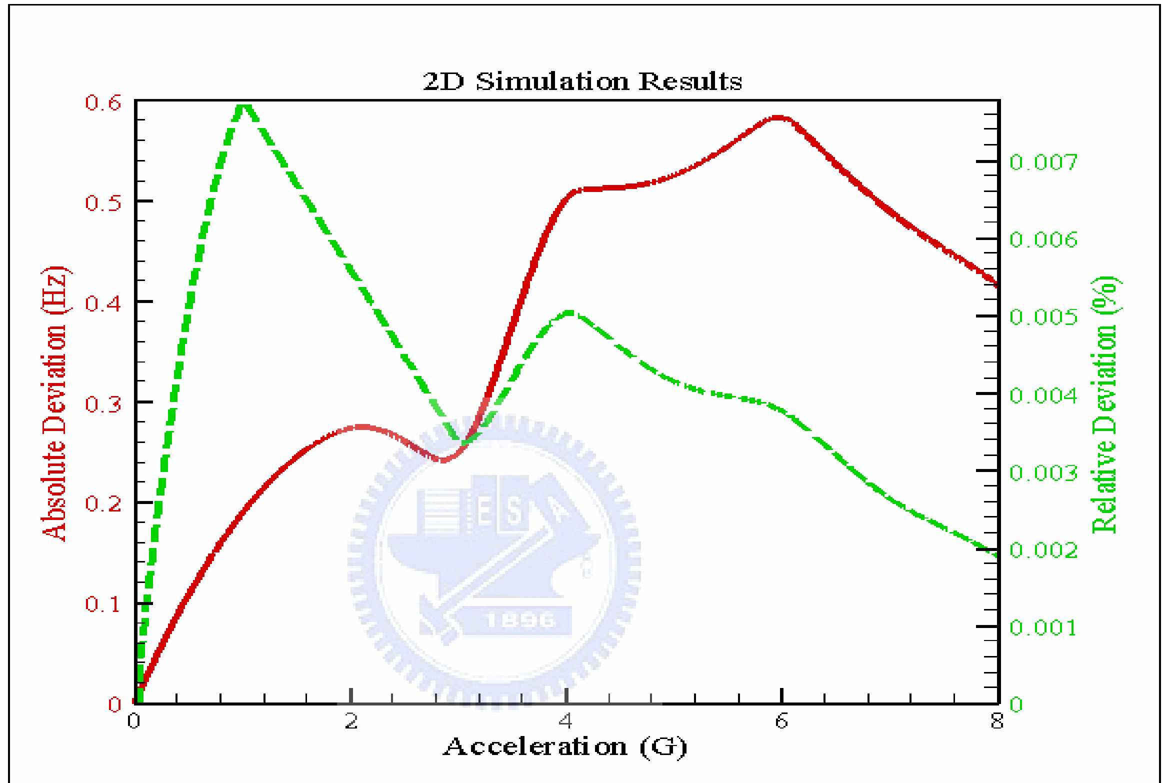

Figure 17. The little deviation between the analytical simulation and FEA indicates the good decoupling capability.

3.6.4. Cross-Axis Sensitivity Evaluation

According to evaluation results shown in Figure 18, the cross-axis sensitivity between the X and Y sensing directions is less than 0.002% for the measurement range from 1G to 7G. That indicates the symmetry structure not only can successfully decouple the planar acceleration, but also the deformation is little even under larger acceleration, implying the structure is reliable to precisely measure the acceleration to a

quite large range.

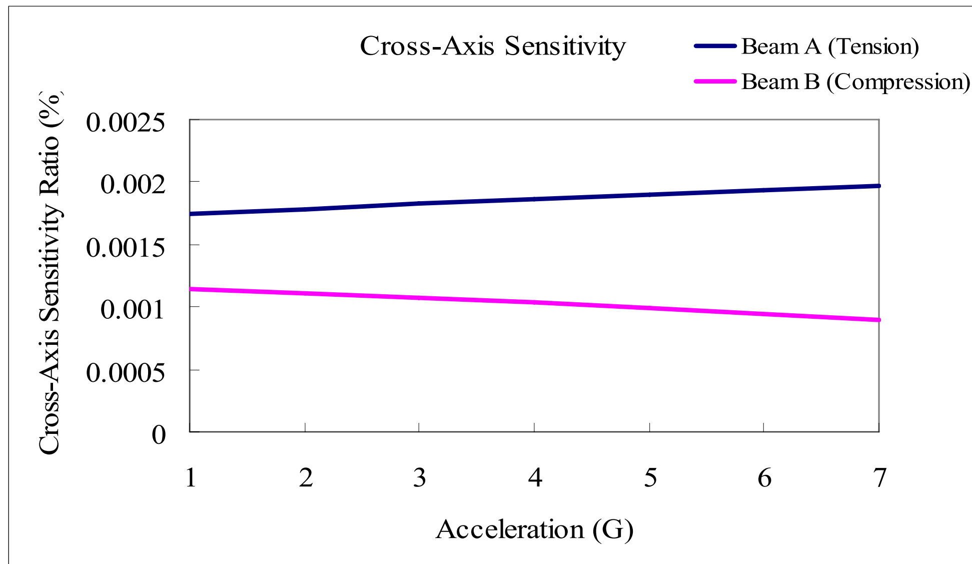

Figure 18. The largest cross-axis sensitivity between X and Y directions is less than 0.002%.

3.6.5. Rigidity Evaluation

The FEA result in Figure 19 also shows that, the vertical deformation of the proof mass due to gravitation is less than 0.507×10^{-3} μm, it indicates that the structure with high-aspect ratio can reduce the vertical deformation.

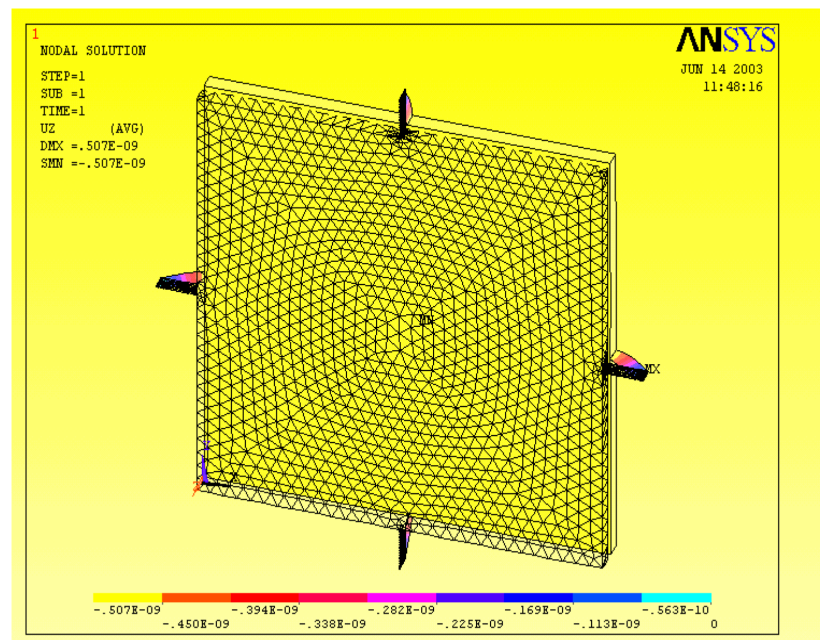

Figure 19. The FEA simulation shows the maximum Z-directional displacement of the proof mass under 1G is about 0.507×10^{-9} m.

3.7. Verification of Analytical Model with Experiment Data

The experimental data listed in Table 5 from conventional DFSM microbridge design [5], as shown in Figure 20 is used here to verify the derived analytical model. By substituting the material properties and geometrical parameters in Table 5 into the analytical model, the natural frequency shift under different accelerations can be obtained, as shown in Figure 21. It shows that the calculated sensitivity – Natural Frequency Difference of 160 Hz/G agrees with experimental result well, which further verifies the analytical model.

The calculation result also shows that, the constraint bridges used to alleviate the displacement in Z-directional acceleration, e.g. gravitation for the proof mass of the DFSM, also reduces the inertia effect of the proof mass from 1.45 mg to 0.4186 mg. However, in our proposed HAR microbeam design, the constraint microbridges are no longer needed, the effective proof mass will not be degenerated. In addition, the exciting and sensing electrodes are placed at two sides of microbeams instead of placing on the substrate beneath the microbridge [5], thus the capacitor area can be enlarged.

In order to identify the enhancement of the proposed design, Table 6 compares the performance between current design having microbeam with dimension of 250 μm long, 1.6 μm wide and 100 μm thick and previous DFSM design having microbridge with dimension of 250 μm long, 100 μm wide and 1.6 μm thick [5] by using the same proof mass of 1.45 mg. It can be found that the capacitor area is 3 times larger, and the sensitivity of the proposed 2D frequency-shift microaccelerometer with HAR resonant microbeams are 3.46 times higher than that of DFSM. Also the displacement of proof mass due to Z-directional gravitation can be reduced from 1 μm to 0.507×10^{-3} μm, as shown in Figure 19. It is evident that the proposed HAR microbeams design is effective in enhancing sensitivity and rigidity over the conventional constraint bridges design.

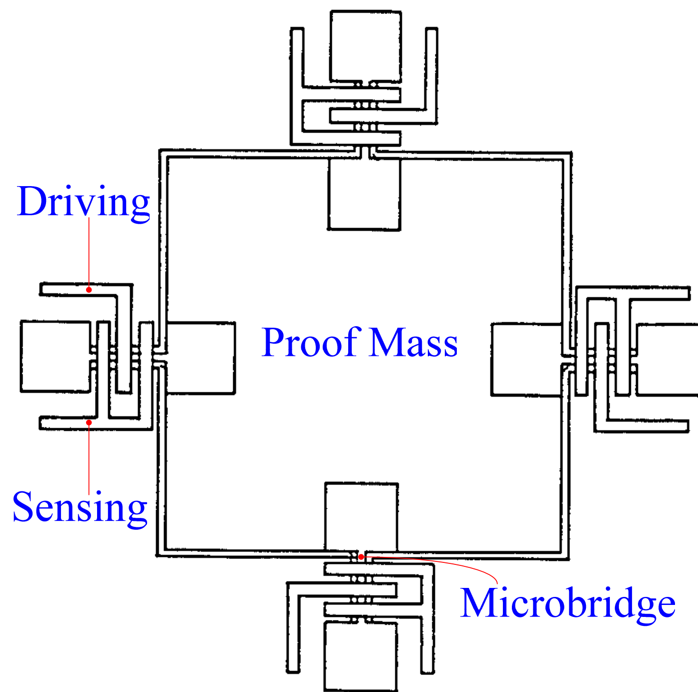

Figure 20 (a). Top view of Chang's 2D frequency-shifted microaccelerometer

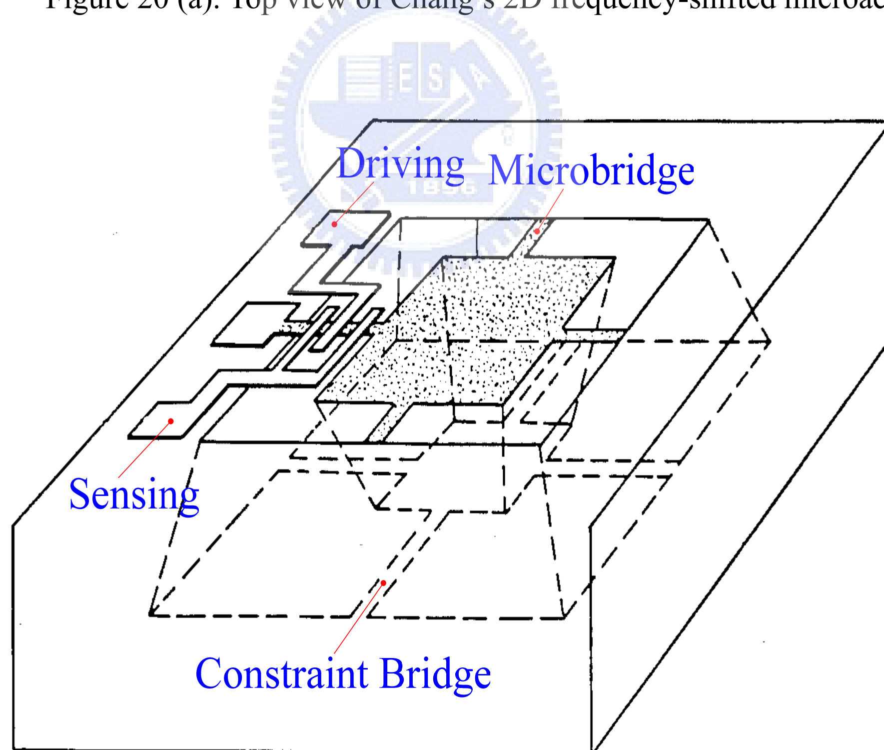

Figure 20(b). Elevation view of Chang's microaccelerometer.

Figure 20. Change's dual-axis natural frequency-shifted microaccelerometer (DFSM) [5].

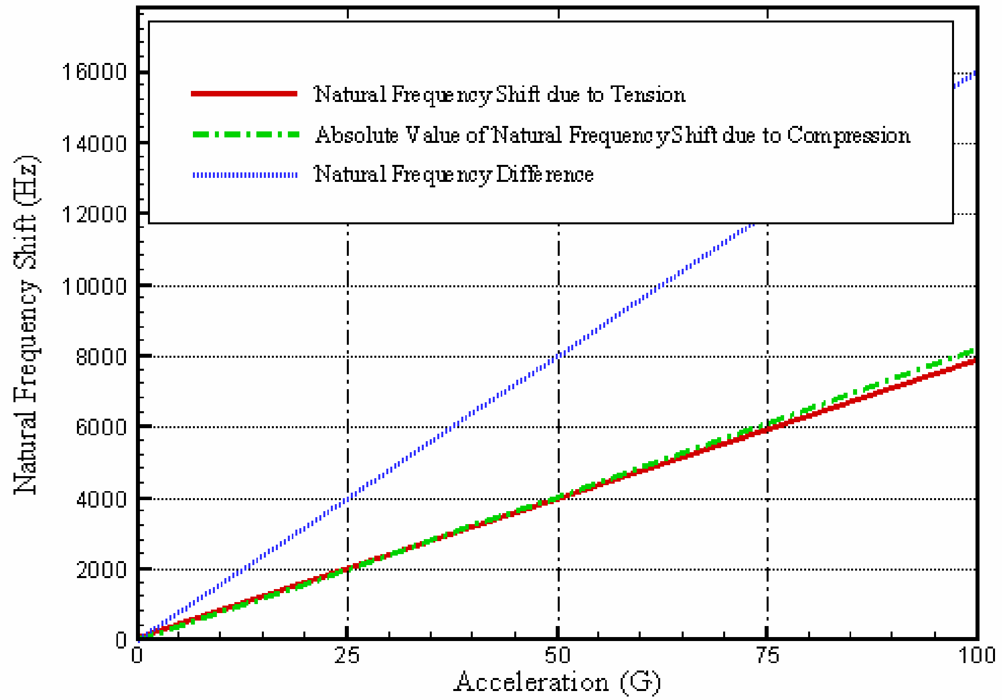

Figure 21. Frequency evaluation of the DFSM [5] using the derived model, the sensitivity is 160 Hz/G.

Table 5: Experimental data in reference [5]

Material	Polysilicon
Young's Modules E (Gpa)	100
Mass Density ρ(Kg/m^3)	2300
Proof Mass (mg)	1.45
Effective Proof Mass (mg) (due to 8 constraint bridges)	0.4186
Dimension of Microbridge (μm)	Length *l*: 250 Width *w*: 100 Thickness *h*: 1.6
Maximum detectable acceleration	1050 G
Natural frequency (kHz)	173
Sensitivity (Hz/G)	160

Table 6: Performance comparison between DFSM design [5] and the current design

	Results of DFSM :	The current design
Capacitor Area	$1/3\times250\times100\mu m^2$	$250\times100\mu m^2$
Structural Rigidity (displacement in Z direction at 1G)	$1\mu m$	$0.507\times10^{-3}\mu m$
Sensitivity	160 Hz/G	555 Hz/G

3.8. Summary

Here a HAR 2D resonant microbeam accelerometer is proposed and analyzed. The simulation shows that the proposed structure is able to decouple a planar 2D acceleration into two independent acceleration components, and the established analytical model is able to evaluate 1D acceleration. FEA for 1D and 2D acceleration simulations are also performed to validate this analytical model, and the agreement between the analytical results and FEA simulation implies not only the cross talk is negligible, but also the assumed fixed boundary condition influence little on the simulation result, meaning that the proposed structure is able to decouple a 2D acceleration and the derived 1D analytical model is therefore can be used to evaluate 2D acceleration. In addition, the experimental results from the conventional microbridge design further verify the accuracy of the current model. From our simulation results, the proposed 2D resonant microbeam accelerometer is more sensitive and also more rigid than the conventional constraint bridges design. It also reveals that the dimension arrangement has direct influence on natural frequency shifting as well as the detecting sensitivity. Hence, the dimensions of the proof mass and the microbeams can be further optimized.

Chapter 4
Fabrication

A systematic recipe set is developed for the adopted UV-LIGA process to process SU8-5 photoresist to fabricate a microaccelerometer structure with high-aspect-ratio. The disclosed recipe set comprises a series of relative recipes for processing SU8-5, including spin speed, soft bake, exposure dose, post exposure bake and developing time. The recipe set is capable of processing SU8-5 film with thickness from 5μm to 80μm. General hot plate, Karl Süss Gyrset spinner RC8 CT62 (spin coater) and MJB3 exposure aligner the frequently adopted equipment in the traditional IC lab, are used to develop these recipes. To verify the recipes, the SU8-5 mold fabricated according to the presented recipe set is employed to electroplate the structure of the 2D microaccelerometer with critical dimension of 4x20x500μm. The detail and most effective process parameters described in this systematic recipe set promote the beginner to process SU8-5 and fabricate the SU8-5 micromold. In addition, various failure reasons due to adopt the improper recipes are also discussed to guide the reader to develop and approach their own proper recipe to process SU8-5.

4.1. Fabrication Consideration

MEMS comprising structures with high-aspect-ratio is interested in recent years, and therefore various kinds of approaches are developed to meet the requirement. However, owing to the conventional equipment such as the spin coater and the UV-aligner are available in the traditional IC lab to process SU8 [23], UV-LIGA process using SU8 photoresist is accordingly became one of the most popular approaches been adopted to form a micromold for electroplating the microstructure.

Though, there are many references in regarding to the process of SU8 [9, 24, 25]. However, a systematic approach including detail recipe for processing the SU8 is still lack. Thus, this work aims at developing a systematic recipe of wide range, which can process NANO™ EPON SU8-5 to form films with thickness ranged from 5 to 80 μm [26]. This SU8 film is used as a micromold to electroplate the microaccelerometer structure [19, 27~29], as shown in Figure 5. For reference, the developed recipe with regarding to spin speed, soft bake, exposure dose, post exposure bake and developing time are all presented in detail. In addition, a microstructure with dimension of 4×20×500μm is built to verify the presented recipe.

4.2. Introduction of SU8-5 Photoresist

NANO™ XP SU8-5 is a negative radiation sensitive resist, which is now commercialized by the company MCC (Micro Chemical Corp.) in USA. According to the information from MCC, SU8-5 contains wt. 52% organic solvent GBL (gamma-butyrolacton). The range of available thickness for the SU8-5 film is from 125 μm to 15 μm corresponding to the spin speed from 250 rpm to 1450 rpm of the spin coater. Additionally, the developer used to develop the post-exposure-baked SU-8 film is an organic solution, which is also supplied by MCC.

4.3. Experiment Equipment and Substrate

For processing SU8-5, the adopted equipment includes Oven; Karl Süss Gyrset spinner RC8 CT62 (spin coater); Karl Süss MJB3 exposure aligner having illumination power intensities of 10 mw/cm^2 for 405 nm, and of 17 mw/cm^2 for 360 nm wavelength; and (4) Hotplate. In addition, α-stepper; Micrometer; Optical microscope; and SEM are employed to inspect SU8-5 patterned film.

4.4. Fabrication Process

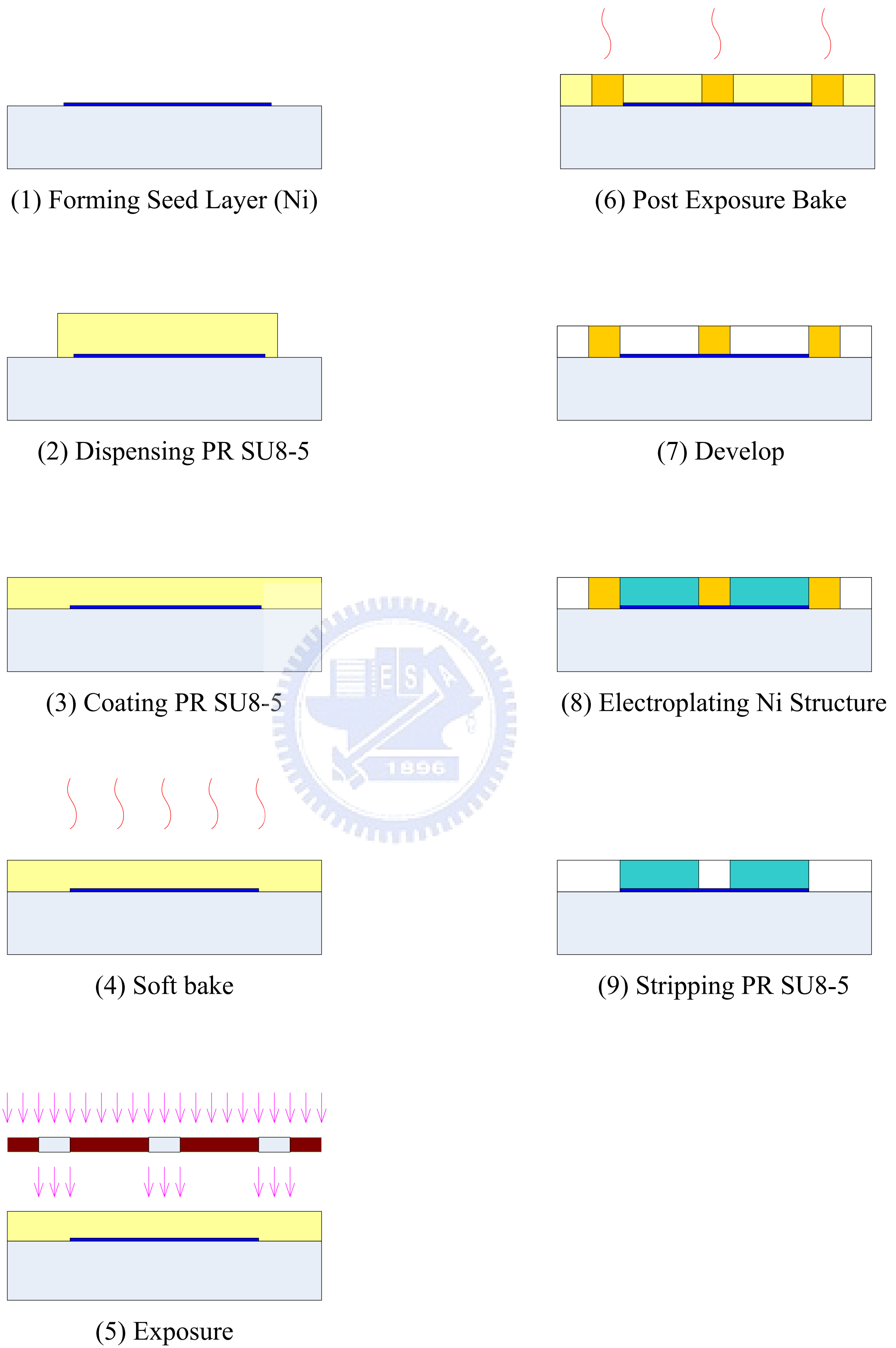

Figure 22. Steps for processing SU8-5.

In this work, the employed substrate is a silicon wafer with 4” diameter, and the environment temperature for processing the SU8-5 photoresist is 24℃.

The procedure to pattern the micromold, comprises following steps shown in Figure 22:

(1) Dispense the SU-8 photoresist onto the substrate

Distribute enough SU8-5 manually and to form a uniformly round region covered with SU8 on the silicon substrate from its center to about 0.6 to 0.8 times diameter, in order to coat films with thickness within the range from 5 to 80 μm. However, a poor SU8 distribution is happened over the entire substrate surface after spin coating, if dispensed insufficient or not uniform SU8 on the substrate.

(2) Spin coating

Spin speed and duration time are two major concerns for coating SU8 film to a demanded thickness on the wafer. The thickness of the SU8 film is not only related to an adopted spin speed but also its duration time. In general, under the same spin speed, the SU8 film becomes thinner as the duration time is taken longer. However, for the identical spinning duration, the film thickness is inversely proportional to the spin speed. Additionally, the uniformity of the film’s thickness is also affected by the duration time. That is, an insufficient spinning duration will cause SU8 transiently distributed on the substrate. Thereby, a thickness variation of the coated SU8 film appears. Figure 23, lists the relation between the SU8-5 film thickness and the spin speed, which is similar with that recommended by MCC. However, it also indicates that, it is difficult to coat precisely a SU8-5 film with thickness over 60 μm, since the curve slope of the film thickness versus the spin speed changes abruptly for spin speed less than 300 rpm. In

addition to spin speed and duration time, environment temperature while processing the SU8-5 is another factor has to be concerned. Since the viscosity of SU8 is decreased as the environment temperature increases. The thickness of the coated SU8 film is also decreased in higher temperature. It is easy to realize that the relation shown in Figure 2 will be deviated under different environment temperature.

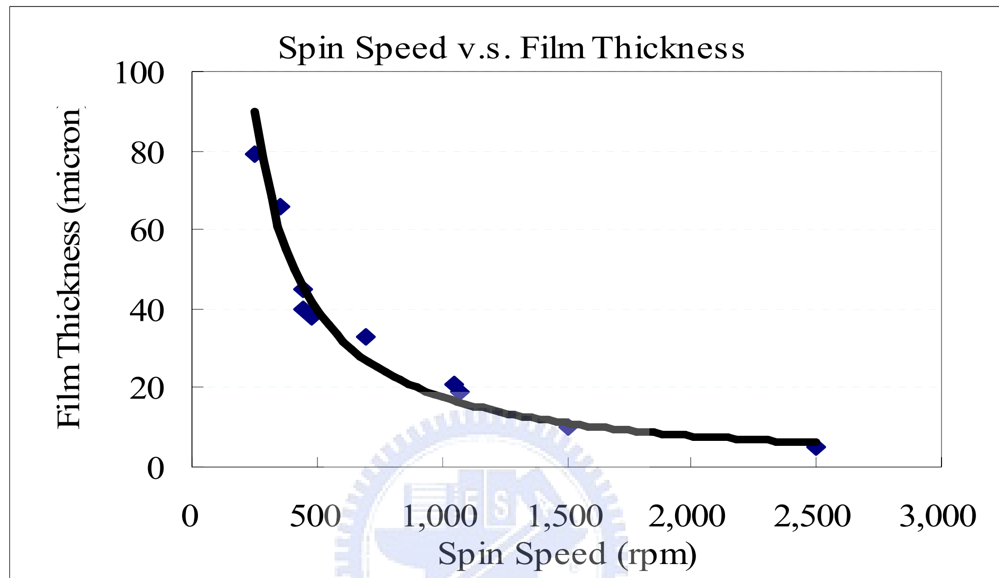

Figure 23. Spin speed and film thickness.

(3) Soft bake

Although, MCC has recommended the baking temperature of 90 ~ 95℃ to cure SU8. However, the time required to soft bake SU8 film with different thickness related to the adopted spin speed is not available. In our work, the soft bake temperature used in this experiment is kept at 90℃. The SU8-5 is just soft baked by hotplate, no forced convection surrounding the SU8 film adopted to facilitate the solvent evacuation. Further, for avoiding the heat shock, a filter paper is spaced between wafer and hot plate for about 3 minutes after the initial contact. In addition, the hotplate has to be well leveled, otherwise, a tilted hotplate makes the SU8 photoresist to redistribute during soft bake and a distorted SU8 film is therefore formed over the substrate. The relationship

regarding the thickness versus required time for soft bake is shown in Figure 24, which including the using the filter paper as a spacer for the first 3 minutes. It shows that, for properly curing the SU8 film, there is a linear tendency relation between the thickness and the soft bake time. In this work, a tweezers is used to touch the cured surface of the SU8 film to inspect the film solidity. If the surface of the cured SU8 film is little deformed by tweezers in gentle touch, the SU8 is cured properly. Otherwise, there has un-negligible residual solvent in the baked SU8. It is found that, an insufficient soft baking cannot properly cure the SU8, the residual solvent will affect the absorption of the exposure energy for the SU8 in the exposure process. On the other hand, if the SU8 is over baked, the cracks appeared at the interface between the substrate and the SU8 film will degrade the adhesiveness. That will make the patterned SU8 film to be lifted off during or after development process.

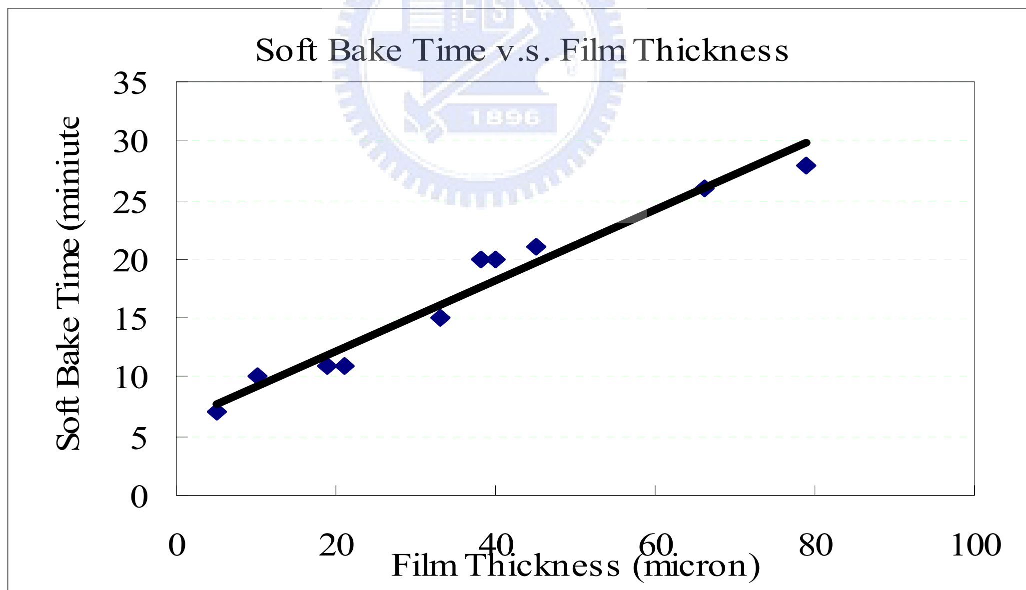

Figure 24. Soft bake time and film thickness.

(4) Exposure

To construct the vertical sidewall on the pattern made of SU8, it has to supply enough exposure energy. Otherwise, insufficient exposure dose cannot offer enough energy to crosslink the exposed polymers in the resin of the SU8. That results in the

exposed SU8 film cannot endure the encroachment from the developer during development and thereby deforms. Contact printing is adopted for exposure to alleviate the diffraction effect, and a longer exposure time or higher exposure dose is preferred to process the SU8 film to achieve a well defined structure with vertical sidewall and sharp corner. Similar to the typical negative photoresist, the relation between the exposure time (dose) and the thickness of the SU8-5 film tends to a slightly nonlinear, as shown in Figure 25. The curve in Figure 25 indicates the minimum exposure dose required for the SU8-5 film with different thickness. To achieve a successful exposure, it has to supply exposure dose higher than that shown in Figure 25 to pattern the SU8. However, an overdose makes the stripping of the SU8 mold more difficult, after electroplated the metal structure.

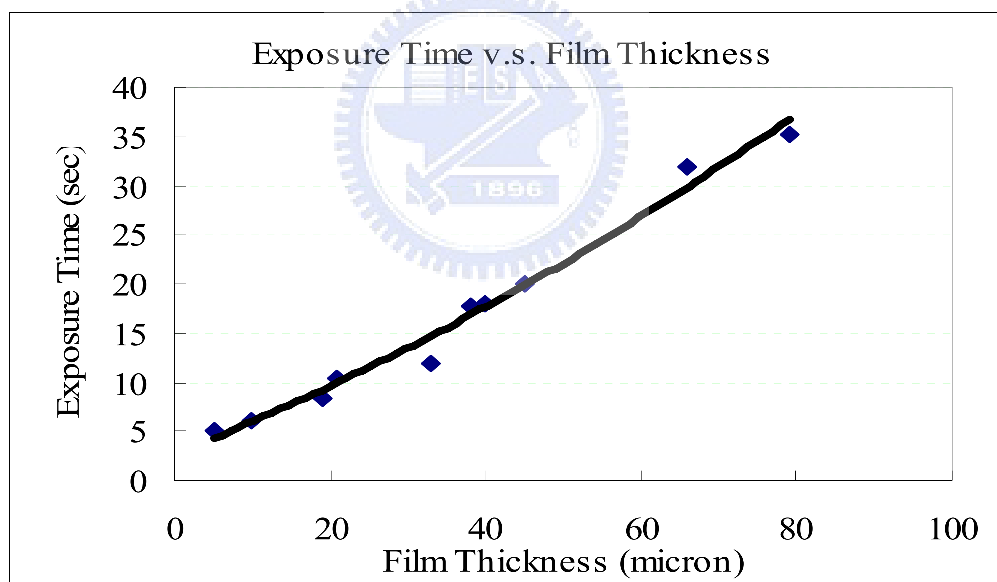

Figure 25. Exposure time and film thickness.

(5) Post Exposure Bake (PEB)

Dose of post exposure bake is critical for successfully defining the pattern on the SU8-5 film. For negative photoresist SU8, PEB is to facilitate the crosslink between the exposed polymers. An insufficient PEB causes the SU8 structure not strong

enough to withstand the encroachment applied by the developer. However, an overdosed PED makes a low selectivity between an exposed and an unexposed region on the SU8 film during development, thereby distort and misshape the pattern of the SU8 film. To define a sharp and clear pattern, Figure 26 shows the adopted PEB time at 90℃ for the SU8-5 film. A break of 3 ~ 5 minutes between PEB and development is necessary to allow a chemical reaction for crosslinking the exposed polymer in the SU8.

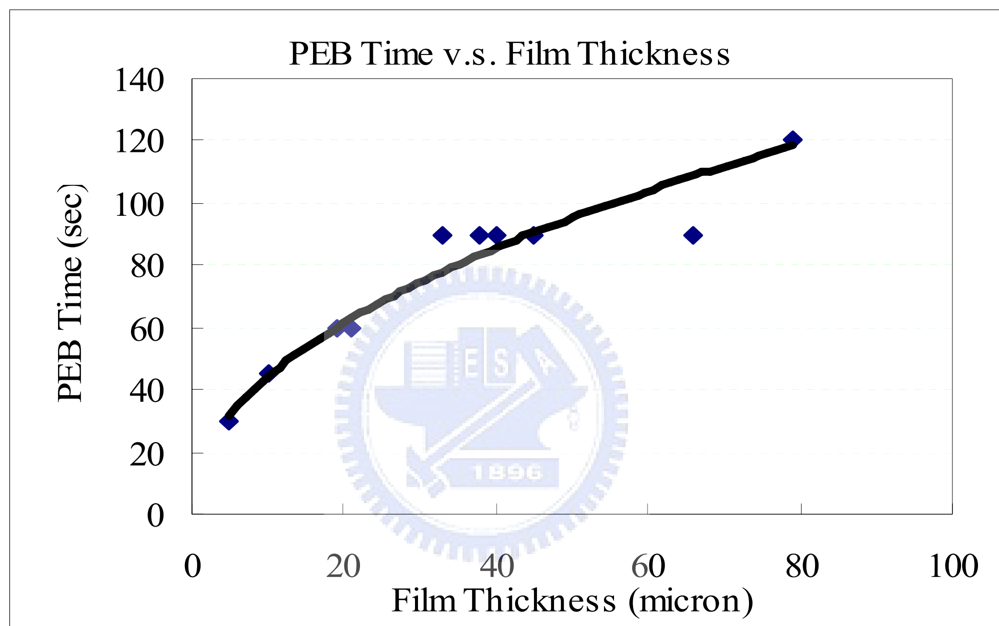

Figure 26. PEB time and film thickness.

(6) Development

Development is to chemically remove the unexposed portions of the SU8 film. By gentle shaking, the exposed portion of the SU8 film on the wafer immersed in the developer lifts off completely from the substrate during a primary development. Fresh developer is used to rinse the wafer has been primary developed for less than 30 seconds to clean the residual scum on the wafer. Thereafter, compressed dry air or nitrogen is used to blow the residual developer away from the substrate. However,

similar to the typical negative photoresist, SU8 absorbs developer and swells during development. Especially, when the solvent in the SU8 has not been adequately removed by soft bake, or the develop time is taken too long. That is, the developer will keep going to encroach on the SU8, and the residual solvent makes the SU8 absorbing more developer and swelling worse. Thereby, the SU8 pattern is distorted. The purple or deep blue scum resulting from the encroached SU8 is appeared on the substrate after development. Figure 27 shows the time adopted for developing the SU8 film, which including the rinse time after the primary development.

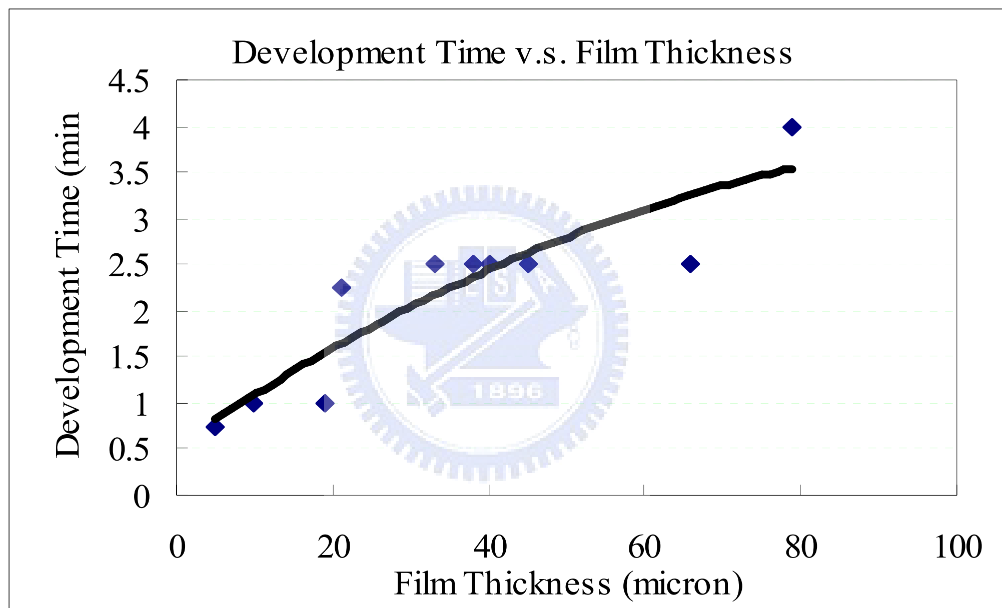

Figure 27. Development time and film thickness.

4.5. Problem and Solution

Figure 28 displays the distorted SU8-5 structure, in which, the swelling structure, the snaking beam and the misshaping gap are due to the developer absorbing. The scum (purple or deep blue color) on the substrate nearby the SU8-5 structure is resulted from the ill soft bake and/or the insufficient exposure dose. The residual solvent in the former makes the SU8 not photosensitive in exposure. However, the later causes less

energy to crrosslink the exposed polymer that inducing the SU8 structure is too weak to resist the developer's attack [30].

SU8 structures in Figures 28 and 29 are configured on the identical silicon wafer. In contrast to Figure 28, structure in Figure 29 indicates that if an incorrect recipe is employed for SU8, the dimension resolution is going to be sacrificed.

When adopting an insufficient exposure dose, the energy transmitted through the SU8 film is not enough to crosslink the polymer, thereby the encroachment is unable to be avoided during development. Figure 30 shows the stain appeared after develop, and Figure 31 shows the SU8-5 structure having an encroached bottom due to an ill exposure dose. When a proper exposure dose is applied, the encroachment is eliminated and the structure is well electroplated, as shown in Figure 32.

4.6. Fabrication Results

Figures 33, 34 and 35 show the structure of the proposed 2D microaccelerometer. This structure is made of nickel, and electroplated by using the SU8-5 mold. The SU8-5 mold has been removed after electroplating. Basically, the recipes shown in Figures 23 to 27 are employed to fabricate this SU8-5 mold. However, the adopted exposure time for the SU8 mold used to electroplate the structure shown in Figures 33 ~ 34 is double to that suggested in Figure 25.

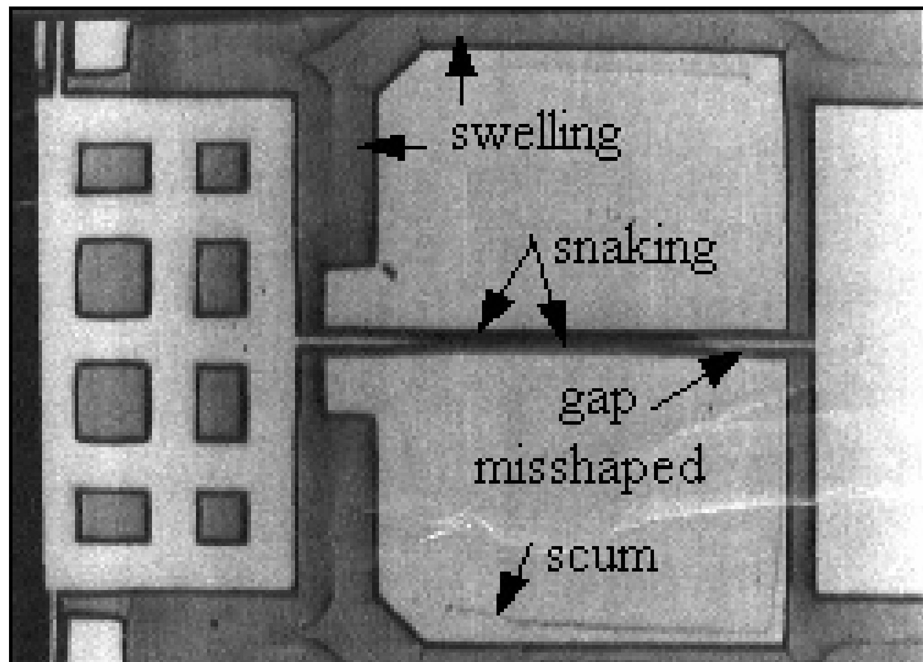

Figure 28. Gap is misshaped due to the snaking structure. The original gap dimension on the SU8-5 mold, is 16 μm width × 1000 μm long × 55 μm deep.

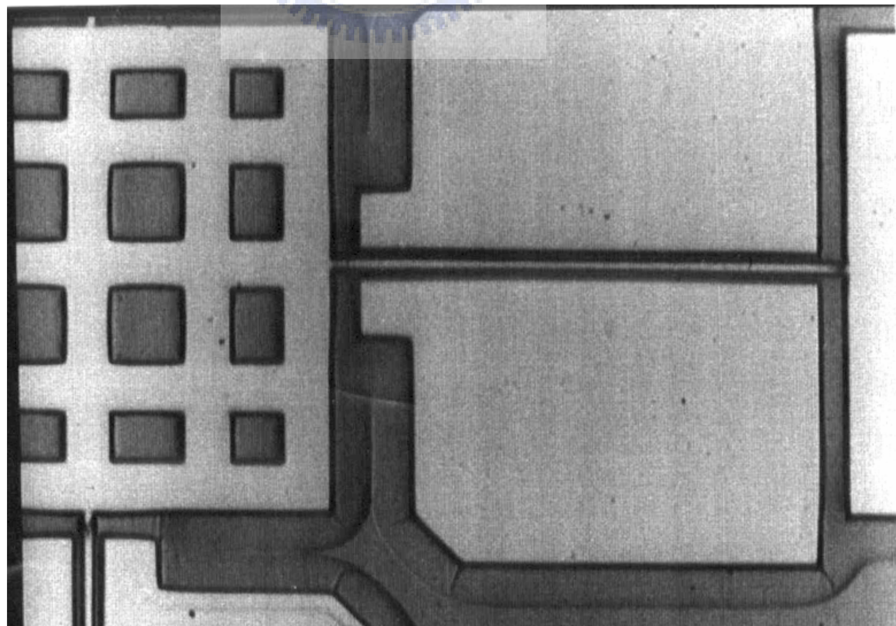

Figure 29. The dimension of gap on the SU8-5 mold, is 18 μm width× 1000 μm long × 55 μm deep.

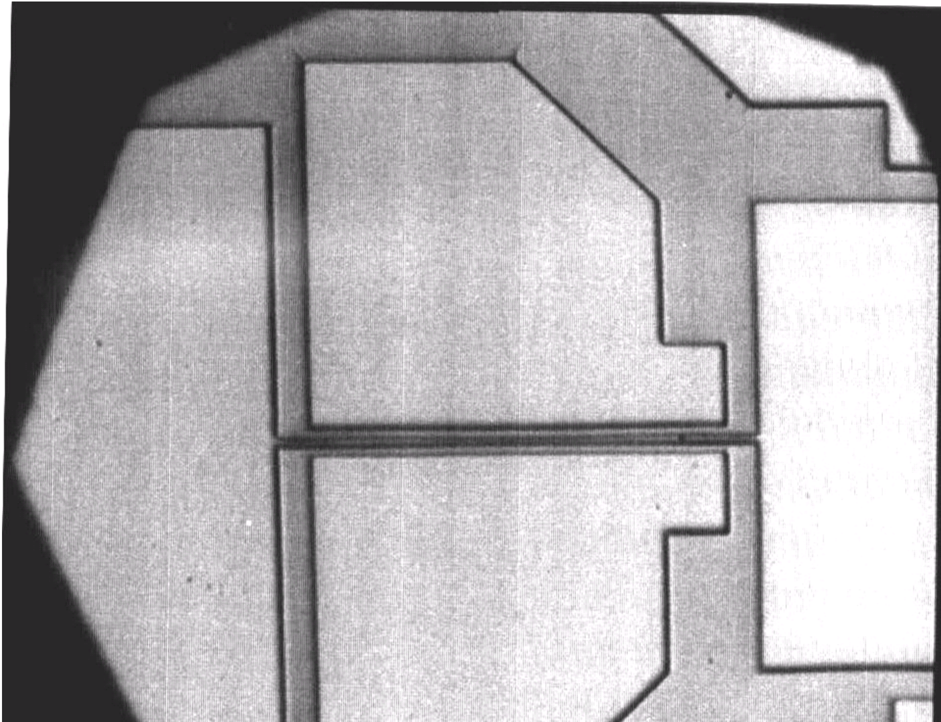

Figure 30. Stain appeared in trench.

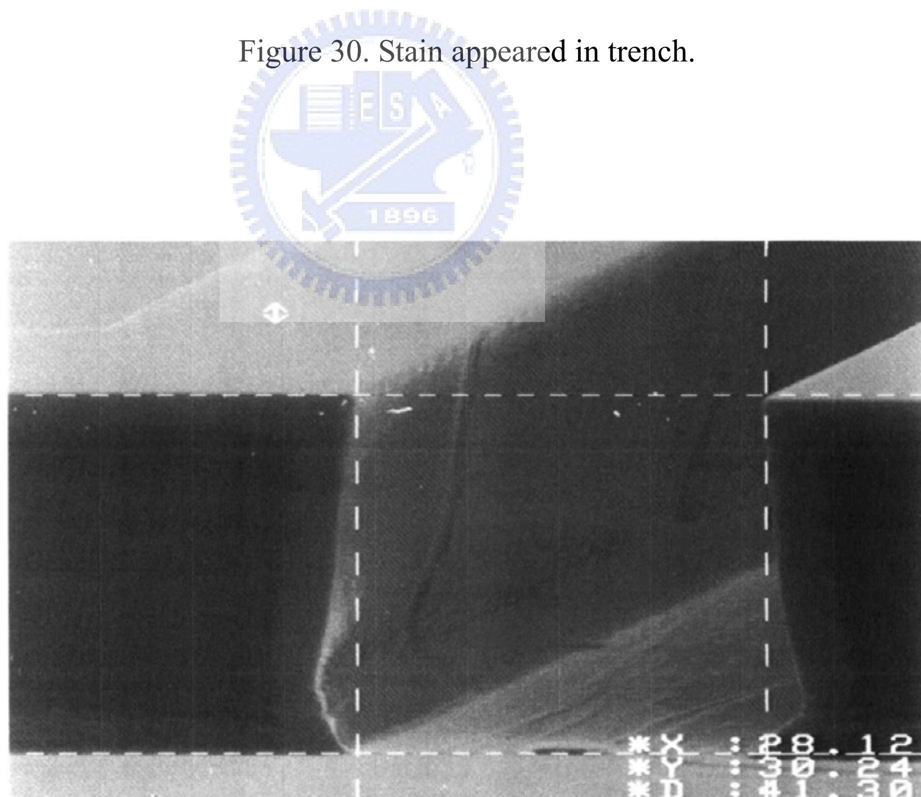

Figure 31. The bottom of the SU8-5 structure is encroached by the developer.

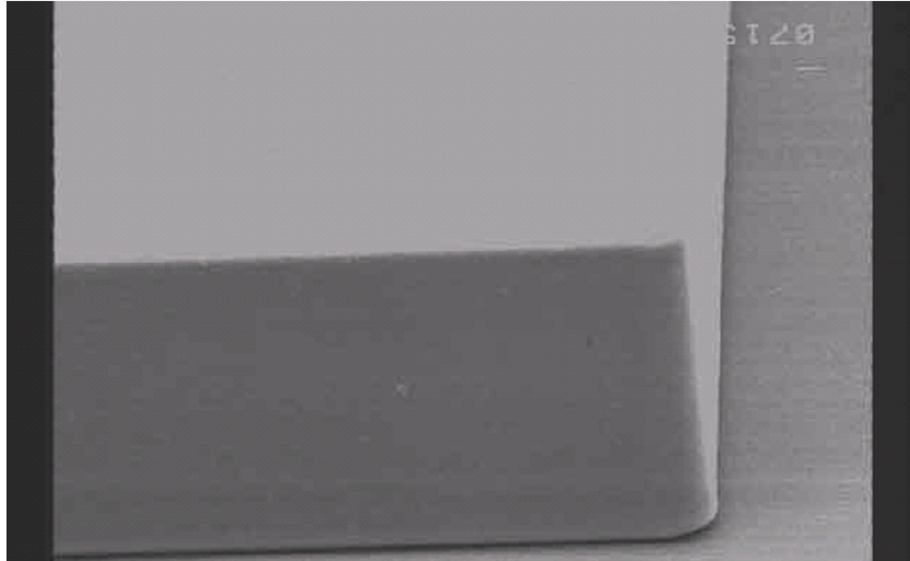

Figure 32. The encroached structure is disappeared by using proper exposure recipe.

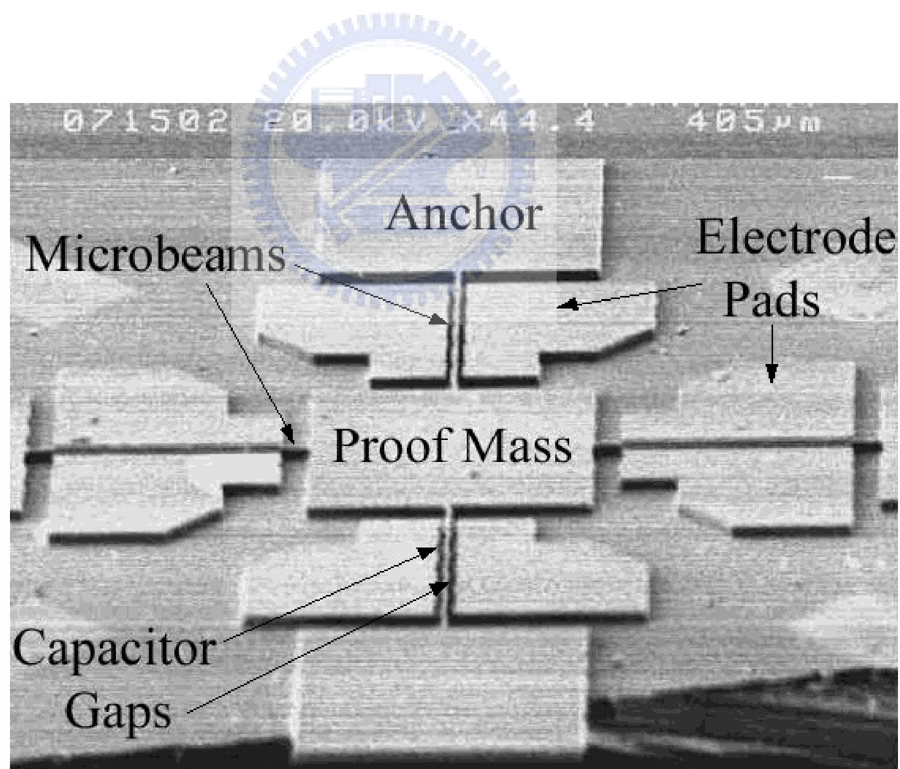

Figure 33. 2D microaccelerometer structure, which is made of Ni using electroplating.

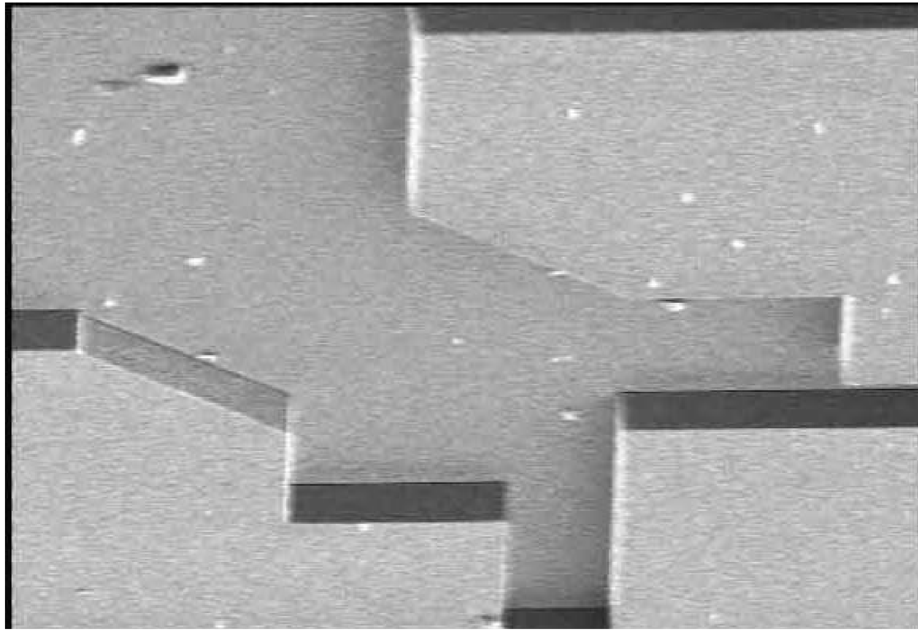

Figure 34. The close-up view of the structure shown in Figure 33.

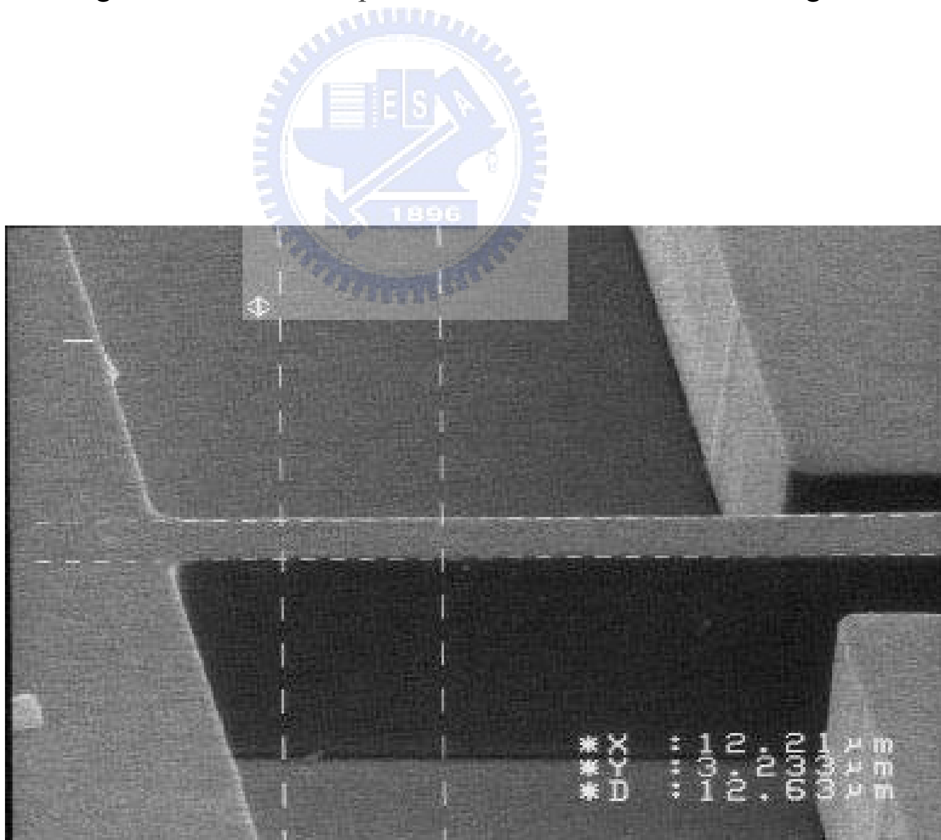

Figure 35. Close up view of the microbeam, electrode pad and their sidewalls. The dimension of the microbeam is about 4×20×500μm.

4.7. Summary

Spin coating, soft bake, exposure, post exposure bake and development are connected together for fabricating SU8 mold. Each individual process described above dominates the fabrication result. In addition to the discussed systematic recipe and dose, the structural geometry of the SU8 is the other factor for achieving successfully fabrication. The SU8 structures shown respectively in Figures 28 and 29 imply, the critical dimension (CD) of a SU8 pattern is not only related to its aspect ratio but also its longitudinal dimension or the slender ratio. That is, under the condition of having identical aspect ratio, a more adequate and precise process recipe is required to fabricate a SU8 structure with longer slender ratio.

Chapter 5
Optimization

In general, the structure of a microaccelerometer is configured with two principal members the proof mass and the spring (beam). The former functions as an active member to response to acceleration and deforms the geometry or changes the physical properties of the accelerometer, such as deformation, displacement, or motion, etc., and the later is to confine or guide the response of the former according to the design consideration. The reaction degree of the proof mass responding to acceleration is always determined by the magnitude of the proof mass and, or the compliance of the spring (beam). That is the sensitivity of an accelerometer with confined geometry size, is a compromise result between the spring flexibility and proof mass magnitude, hence, to raise the sensitivity, the dimension arrangement for the proof mass and the spring (beam) has to be optimized. In this work, to obtain a most sensitive resonant beam microaccelerometer, the analytical model is used to maximize a defined sensitivity function *S* by optimizing the dimension for the microaccelerometer. The evaluation result shows that, as the length of the microbeam length is one half of the width of the proof mass, a maximum sensitivity of 8%/G in the illustrated mciroaccelerometers is achieved.

5.1. Optimization and Sensitivity

In general, a MEMS inertia or force device is constructed by two principal members, one is an energy conversion member e.g. spring or beam to convert between potential and kinetic energy, and the other one is an active member, e.g. proof mass to respond to a physical environment change. When the sensor structure is subject to an external action, such as acceleration or force, the active member reacts accordingly, and deforms geometry or changes physical property of the accelerometer, such as deformation, displacement or motion, etc. However, the reaction degree of the active member - the proof mass is always confined by the potential to kinetic energy conversion member - the spring. That means the sensitivity of the sensor is a compromise between the spring flexibility and proof mass magnitude [31-35]. For the proposed 2D resonant microbeam accelerometer, the microbeams connecting and suspending the proof mass function as springs, and the proof mass is working as the active member responding to an external acceleration and applying on the microbeam an axial force to change a certain physical performance e.g. to shift the natural frequency of the microbeam. The simulation result indicates that, the response sensitivity, such as the shifted frequency of the microbeam due to the detected acceleration, is dominated by the dimension of the structural component i.e. microbeam and the proof mass. That is, the longer, and thus more flexible, the microbeams are, the more sensitive the 2D accelerometer is for a given proof mass dimension [32]; and the larger the proof mass is, the more sensitive is for the device with a given microbeam length. Typically, for a device with geometry constraint, whose total area is fixed, that is, increase the length of the microbeams will also reduce the width also the area of the squared proof mass. Accordingly, there should be an optimum compromise to arrange the dimension for microbeam and proof mass to configure a most sensitive microaccelerometer. To raise the sensitivity of the 2D accelerometer, a sensitivity

function S of geometric parameters is defined and evaluated by using the derived model. The evaluation result shows that, the maximum sensitivity S is achieved, when an optimum geometric dimension arrangement - the length of the microbeam equals to one half of the width of the square proof mass is assigned.

5.2. Dimension to be concerned for sensitivity

Figure 12 shows the geometry of the microaccelerometer. The width of the anchor frame is W. The symbols l and w are respectively the length and the width of the microbeam, and L is the width of the proof mass. The thickness of the proof mass and the microbeam are identical and represented by h as shown in Figure 1(b) in Chapter 2 or 3. These geometric parameters are the major concern for evaluating sensitivity of the microaccelerometer structure.

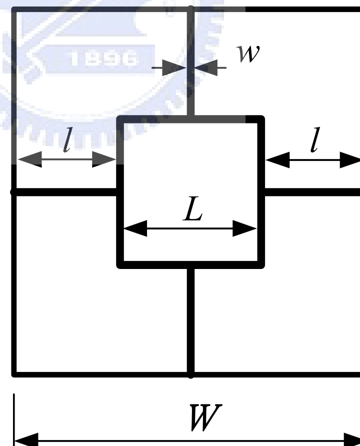

Figure 12. The characteristic dimensions l, w, L to be optimized to raise the sensitivity of the microaccelerometer. (Repeat)

5.3. Definition of Sensitivity Function

The simulation in Chapter 3 shows that, the mechanical sensitivity is connected to the dimensional arrangement for the microbeamand the proof mass. Thus, to investigate the sensitivity-dimension relationship, the microaccelerometers confined by

$W=L+2l$ is considered and evaluated to find an optimal dimension arrangement for the microbeam and the proof mass to raise the sensitivity of the microaccelerometer.

5.3.1. Optimization of Structure Dimension

According to [32] the sensitivity function is defined as

$$S = \frac{\Delta OS}{(OS)P} \tag{14}$$

where OS represents an output signal, and ΔOS is a variation of OS due to an external application P. By imposing a geometric constraint, a maximum sensitivity S can be found.

5.3.2. Structure Dimension Arrangement and Mechanical Sensitivity

In this work, the concerned output signal OS, the signal variation ΔOS, and the external application P shown in Eq. (14) are respectively the natural frequency f_0 of microbeam, the frequency shift due to one G variation, i.e. $\Delta f(G)$, and the acceleration G. The connection between f_0 and $\Delta f(G)$ is shown in Eq. (15), and Eq. (14) can be represented as Eq. (16).

In order to realize how the sensitivity is related to the dimension arrangement for the proof mass and microbeam, some illustrated microaccelerometers with thickness h of 20 μm and confined by the dimension arrangement of $W=L+2l=6000$ μm are evaluated using Eq. (16).

$$\Delta f(G,L,l,w) = f(G,L,l,w) - f_0(L,l,w) \tag{15}$$

$$S(L,l,w) \equiv \frac{\Delta f}{f_0 G} \tag{16}$$

Figure 36(a) displays the result of using Eq. (16) to evaluate the sensitivity function *S*(*L,l,w*) for the illustrated microaccelerometers. It shows that, for the same length, a narrower width induces a more sensitive microbeam. However, the most important result is that, when the length *l* of microbeam (1500 μm) is equal to one half of the width *L* of proof mass (3000 μm), the microaccelerometer is most sensitive. Figure 36(b) is a part of Figure 36(a), which shows that for microbeams having wider width *w*, the maximum sensitivity will decrease. It indicates that there is an inverse proportional relation between the beam width and the sensitivity.

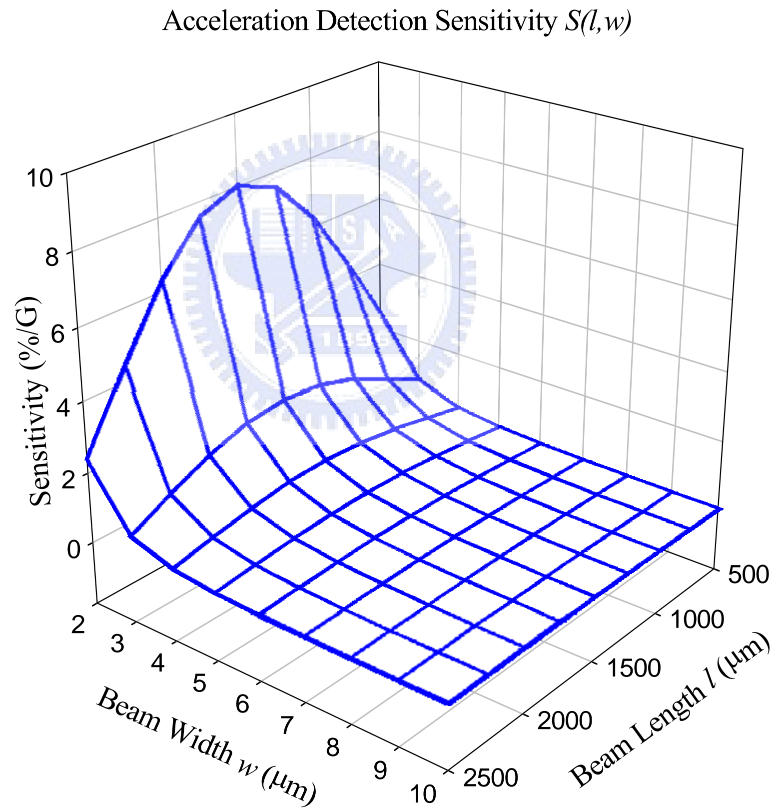

Figurer 36 (a). Sensitivity evaluation for the illustrated microaccelerometers.

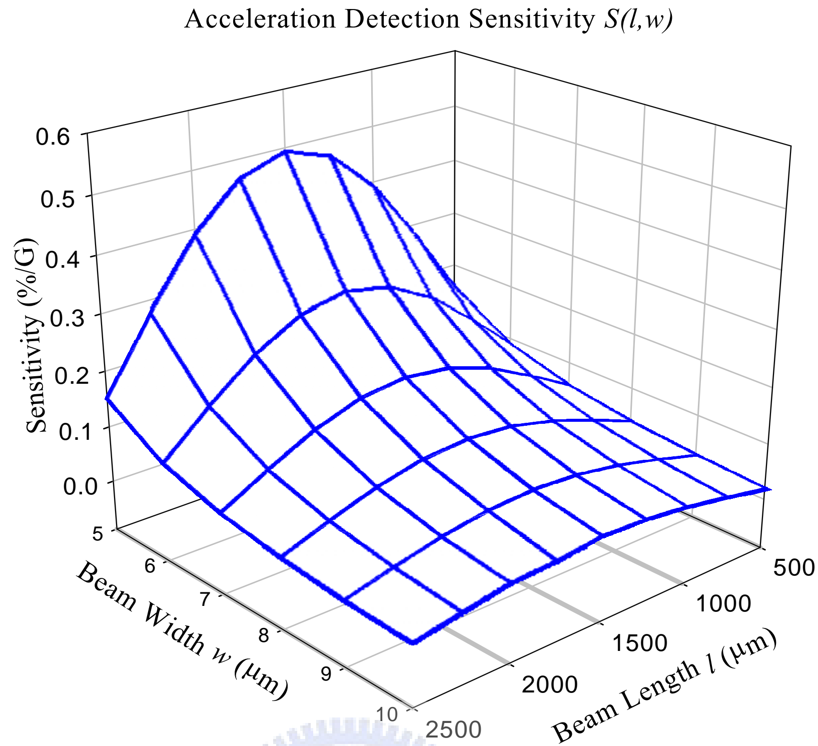

Figure 36(b). Magnifies of Figure 36(a), for microbeams with thickness ranged from 5μm to 10μm.

Figure 36. The sensitivity evaluation of microaccelerometers with thickness h of 20 μm, confined by $W=L+2l=6000$ μm.

In contrast to Figure 36, Figure 37 describes the maximum detectable acceleration, which is limited by the compression of Eq. (11) applied on the microbeam, and the maximum compression has to be less than the buckling loading of the microbeam in Eq. (12). For the same length, although the wider microbeam the dopy is to respond to a small acceleration, it is able to measure a larger acceleration before buckle. In other words, when the sensitivity increases, the maximum measurable acceleration decreases.

$$T_{\max} \cong \frac{M}{2} a_{\max} \qquad (11) \text{ (Repeat)}$$

$$T_{\max} \leq T_{cr} = \frac{4\pi^2 EI}{l^2} \qquad (12)\ \text{(Repeat)}$$

In addition to the sensitivity consideration, it is necessary to design a proper separation between the movable proof mass and the underneath substrate to prevent the proof mass and microbeam from contacting the substrate during operation.

FEA is used to estimate the vertical displacement of proof mass due to Z-directional gravitation or acceleration. Figure 38 shows that, the displacement variation tendency of the proof mass is similar with that of the sensitivity distribution depicted in Figure 36(a), and the maximum vertical displacement of the proof mass also appeared when l equals to $L/2$.

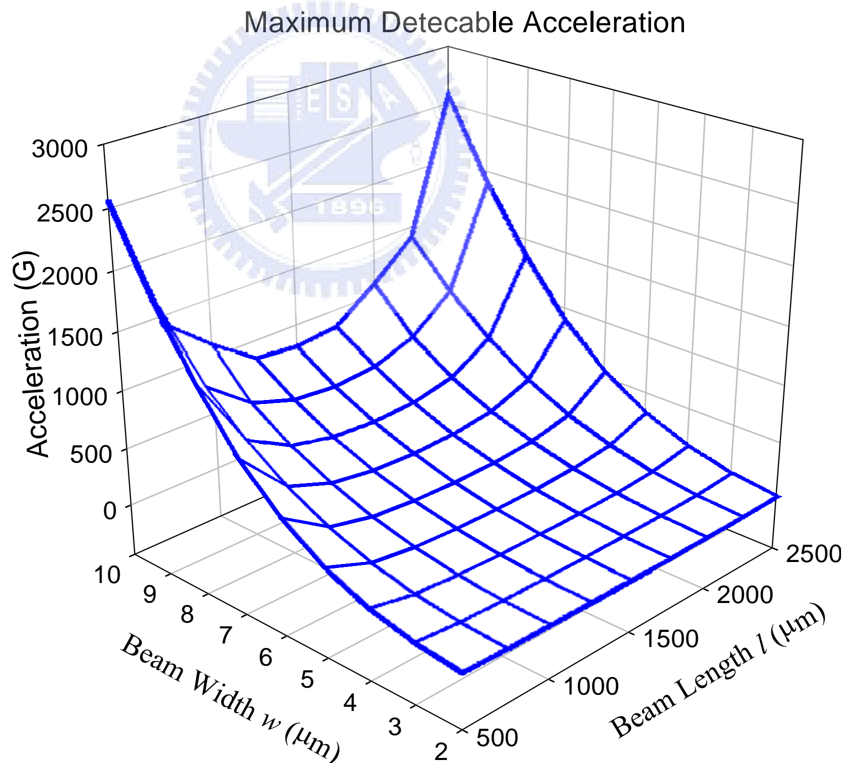

Figure 37. The distribution of the vertical displacement of proof mass due to Z-directional gravitation or acceleration.

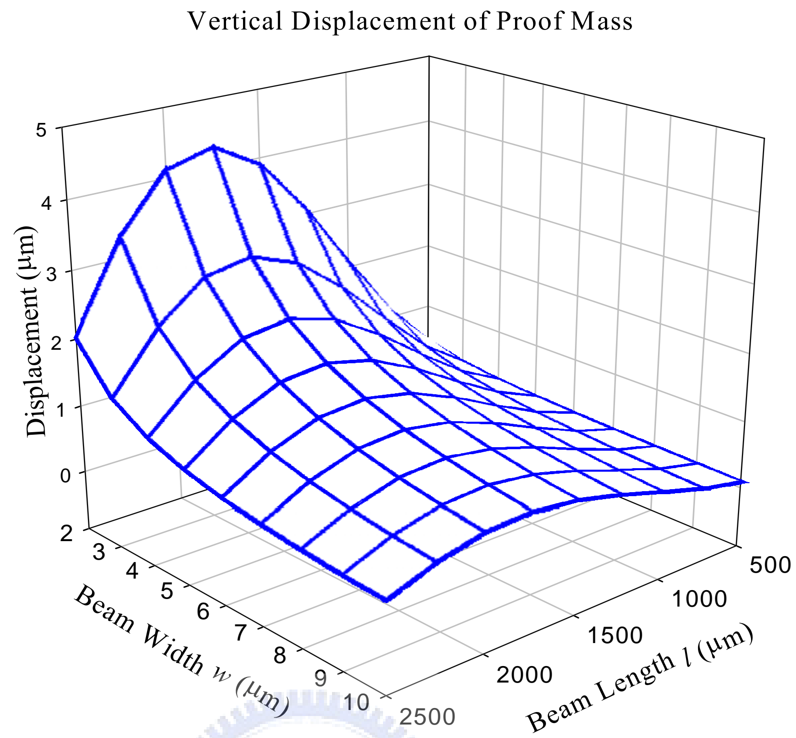

Figure 38. The maximum detectable acceleration for the illustrated microaccelerometers.

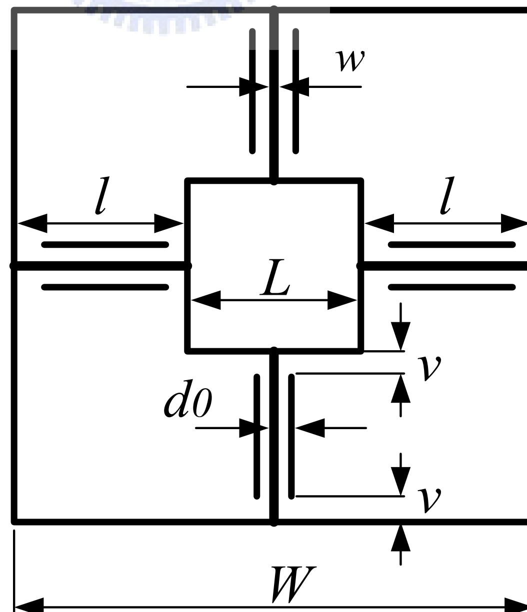

Figure 39. The dimension of the separation v is to be optimized to maximize the capacitance change ratio for the capacitor under a voltage application.

5.4. Optimization for Capacitor Dimension

When a voltage V is applied across the microbeam and the electrode pad, an electrostatic field is established, as shown in Figure 40(a), and an electrostatic force f_e [31] is generated using the hypothesis of the parallel-plate capacitor:

$$f_e = \frac{\varepsilon_0 A_c}{2d^2} V^2 \tag{17a}$$

Where ε_0 is the permittivity constant and A_c is the area of capacitor plate.

By static analysis, the released and movable microbeam, as shown in Figure 40(b), is attracted by the electrostatic force of per unit length q_e, where

$$q_e = \frac{\varepsilon_0 h}{2d^2} V^2 \tag{17b}$$

The deflection curve $y(x)$ of the microbeam, deflected toward to the electro pad is

$$y(x) = \frac{q_e}{EI}\left\{\frac{-1}{8l}(l-2v)\left[v^2 + (l-v)^2 - \frac{2}{3}(l-2v)^2\right]x^2 + \frac{1}{12}(l-2v)x^3 - \frac{1}{24}(x-v)^4\right\} \tag{18}$$

where two distinct separations v shown in Figure 40(b) are respectively used to separate the electrode pad from the proof mass, and from the anchor.

The original gap d_o between the microbeam and the electrode pad decrease to d due to the deflection $y(x)$ caused by the electro static force q_e, and accordingly the original capacitance C_0 is increased to C

Where

$$C_0 = \frac{\varepsilon_0 A_c}{d_0} \cong \frac{\varepsilon_0}{d_0}(l-2v)h \tag{19}$$

and

$$C = \int_v^{l-v} dC \cong \varepsilon_0 h \int_v^{l-v} \frac{dx}{d_0 - y(x)} \tag{20}$$

According to Eq. (17b), when the microbeam deflects toward to the electrode pad, the unit electrostatic force q_e is increased corresponding to the decreasing gap d between the electrode pad and the microbeam. However, according to Eqs. (17b) and (18), under the application of a constant voltage, there should be a transformation between strain energy stored in the deflected microbeam and the work done by the electrostatic force q_e. That is, an initial q_e not only decrease gap between the microbeam and the electrode pad from d_0 to d but also increase q_e itself and the strain energy in the bent microbeam, thereby the interaction of further decreasing gap d and the increasing q_e are finally equilibrium as more strain energy has been stored. However, for a small deflection, the described complex nonlinear phenomena can be simplified by assuming the unit electrostatic force q_e is constant, and varying little as the gap d decreasing. Thus, the deflection curve $y(x)$ of the microbeam caused by the electrostatic force q_e, as shown in Eq. (18), can be estimated by using the classic mechanics of material.

Under the assumption of applying a constant electrostatic force q_e, the change ratio of the capacitance $S(v)$ with respect to the separations v is defined below,

$$S(v) \equiv \frac{\Delta C}{C_0} \tag{21}$$

where $\Delta C = C - C_0$

From Eqs. (17) to (21), it can be concluded that the change ratio of the capacitance $S(v)$ is not only dominated by the gap d and the applied voltage V, but also the separations v.

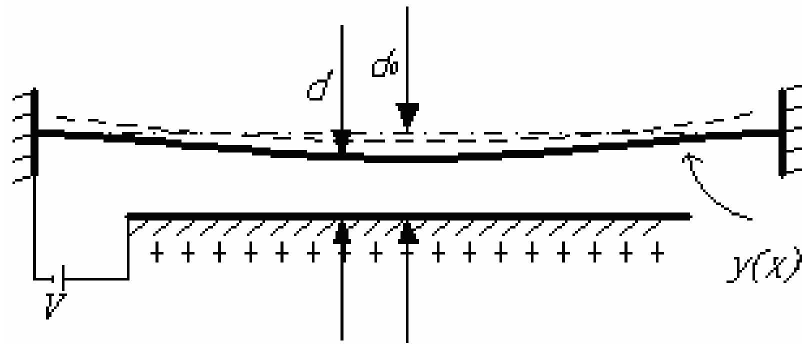

Figure 40(a). Voltage V is applied across the microbeam and the electrode pad, and an electrostatic field is established.

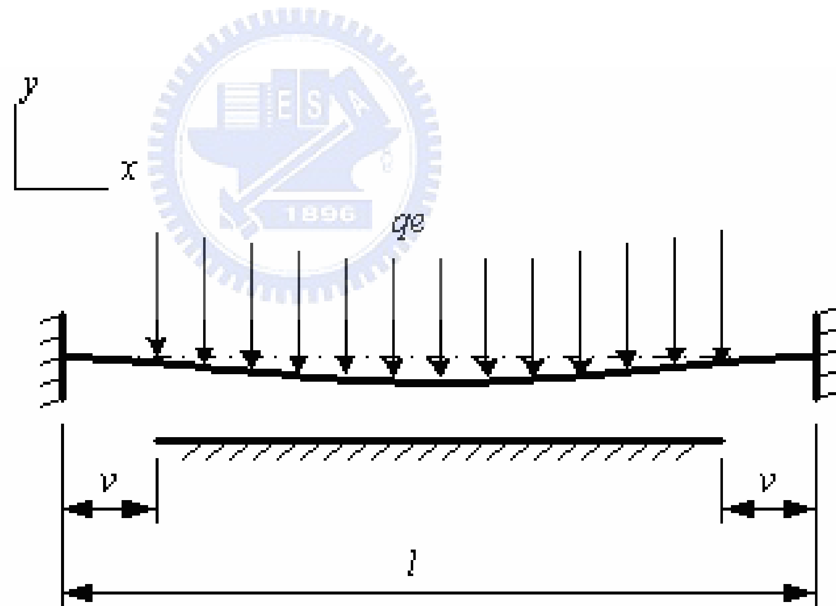

Figure 40(b). The electrostatic force q_e generates and attracts the released microbeam to deflect along the y-direction toward to the electrode pad and forming a deflection curve $y(x)$.

Figure 40. Dimension optimization for separation v.

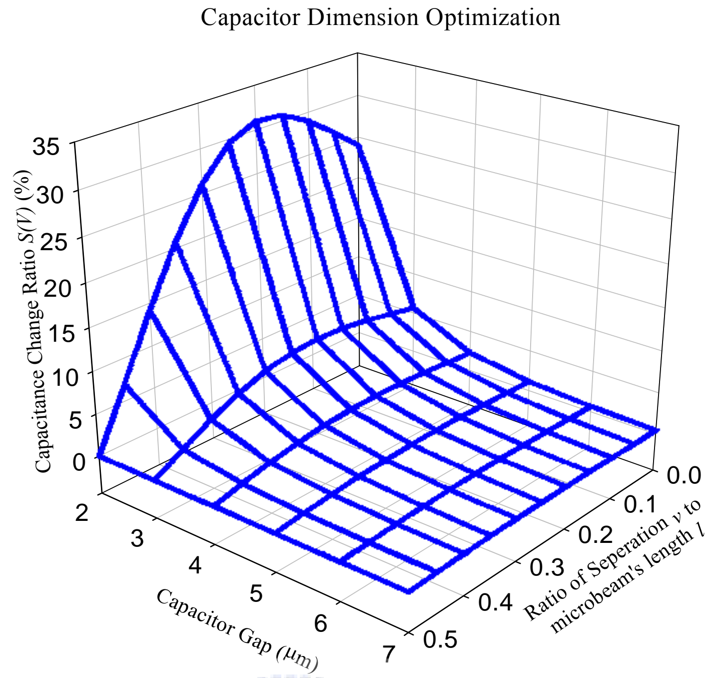

Figure 41. The change ratio of the capacitance $S(v)$ of the capacitor of the microaccelerometer under the application of a voltage at 10V. The length l of the microbeam is 1500μm, the separation v and gap d are respectively ranged from 0.1 l to 0.5 l and 2 to 7 μm.

Figure 41. Shows the change ratio of the capacitance $S(v)$, for the capacitor form by the electrode pad and the microbeam shown in Figure 40, under the application of a voltage at 10V. In this simulaiton, the length l of the microbeam is 1500 μm, which forms the one plate of the capacitor, and the separation v and the gap d are in the range from 0.1 l to 0.5 l and 2 to 7 μm, respectively. In Figure 41, the maximum change ratio of the capacitance appears around $v = 0.15\ l$ to $v = 0.2\ l$ for the given gap d. In general, $S(v)$ increases as the gap d decreases.

5.5. Summary

To design a resonant microbeam microaccelerometer structure with highest sensitivity, a sensitivity function of geometry parameters is defined. The analytical model derived in Chapter 3 is used to evaluate the sensitivity for the proposed microaccelerometer confined by a dimension constraint. The sensitivity evaluation result reveals that, when the length l of the microbeam and the width L of the proof mass have been specified, a microbeam having a narrower width w leads to a more sensitive accelerometer, however, in case of the microbeam width w has been specified, the optimum dimension arrangement to achieve a microaccelerometer with highest sensitivity is to assign the length of microbeam equal to one half of the width of the proof mass.

Chapter 6
Discussion

6.1. Modeling and Geometry

The symmetrical and orthogonal characterizations of the structure makes the proposed microaccelerometer is able to decouple a planar acceleration into two independent components and the compactness of the proposed microaccelerometer shown in Figure 1, let a simple analytical model can be derived to represent the response i.e. the natural frequency shift of the microbeam due to the acceleration. Microbeam with high-aspect-ratio provides itself rigidity to against the gravitation and thereby reduce the deformation due to gravitation. The largest shrinkage of the 1000 μm long microbeam before bulking is about 0.007 μm, and the response of the accelerometer structure induced by the acceleration does not cause any significant geometric deformation but a physical effect, such as the natural frequency variation of the microbeam induced by the axial force, that implies, the little deformation of the structure makes the analytical model always in coincidence with the geometry and the dimension of the microbeam. Therefore the derived model is reliable in acceleration detection.

6.2. Mechanical Sensitivity and Structural Dimension

Typically, the performance of a microaccelerometer is dominated by the designed microstructure [11, 32, 36]. That is, structural geometry, response, electrical reaction region, sensitivity and rigidity of the device are the major factors have to be concerned in designing the microstructure. In design the configuration for the proposed microaccelerometer, the structural geometry is deliberated by qualitatively complying with above factors. However, the dynamic response, such as the linear natural

frequency shift of the microbeams due to the acceleration, is evaluated quantitatively by a derived model and FEA. And the most sensitive structure, the optimal dimension ratio is 1:2 for the microbeam's length to the width of the proof mass. The maximum capacitance change ratio under a voltage application for the capacitor disposed on the sidewall of the microbeam is about v = 0.15 l to v = 0.2 l for the given gap d_o. In general, the capacitance change ratio increases as the gap d_o decreases.

6.3. Fabrication

In addition to the design considerations mentioned above, to verify the capability of manufacturing the microstructure with high-aspect-ratio, a prototype made of nickel is shown in Figures 7 and 8, which is electroplated by using SU-8 mold [10, 11]. Figure 8 demonstrates the degree of freedom of using UV-LIGA process to fabricate the high-aspect-ratio structure. This degree of freedom in fabrication is available to enlarge the capacitor area disposed on the sidewall of the microbeam along the direction of the structural height, and the capacitance is thereby increasable.

Chapter 7
Conclusion and Future works

7.1. Conclusion for Design, Fabrication and Optimization

1. The derived 1D analytical model is verified by FEA.
2. Frequency shift principle is used to get a linear response, and the largest mechanical non-linearity is about 10% FSO (Full Scale Output).
3. Structure with high-aspect ratio is used to enhance the rigidity to resist the vertical acceleration, and the vertical deformation is less than 0.05 μm under gravity.
4. Geometry symmetry can decouple a planar acceleration into two independent components. The cross-axis sensitivity is less than 0.002%, thereby the derived 1D model can be used to evaluate a 2D acceleration.
5. The optimization results show that, when proof mass' width is twice of beam's length, the structure is most sensitive.
6. Dimension optimization can increase the sensitivity up to 8%/G..
7. The electroploated Ni microbeam with 4 μm width show that, the adopted UV-LIGA process can meet the dimension requirement for the microbeam with 5 μm width in simultion.

7.2. Future works

1. Design - Complete the accelerometer system consisting of mechanical structure and circuit.
   - Design the structure dimension according to a practical spec requirement.
   - Dynamics Evaluation and Characterization (Mechanical Plant)
   - Capacitance and Electrostatic Force Evaluation (ME interface)
   - Design and Implement Phase Lock Loop (PLL) circuit; Controller, Electric Hardware
   - Control Algorithm Development; Controller, Software or Firmware
   - Test
2. Fabrication - Use SOI and Adopt DRIE with Anodic Bonding Process

   - NeoStones can offer this process.

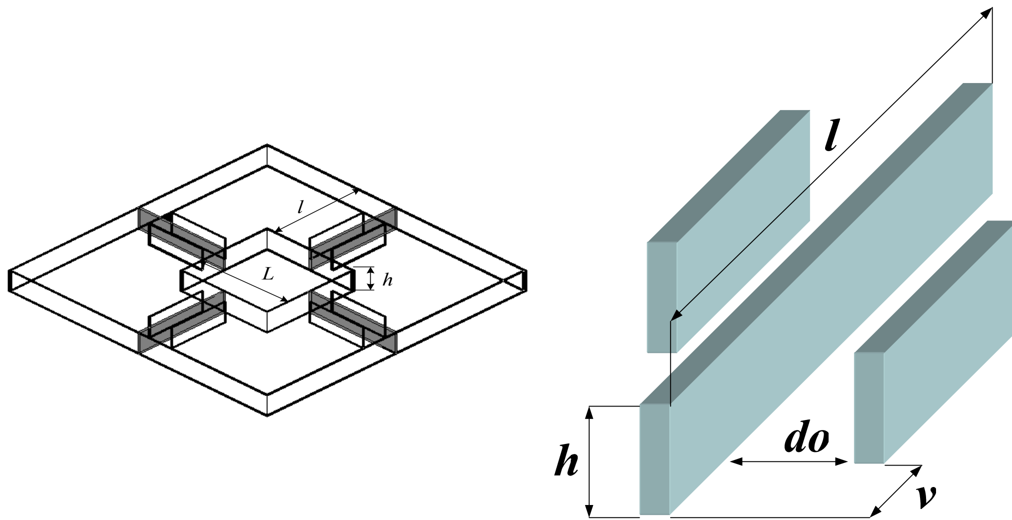

Figure 42 (a). The dimension arrangement of the microbeam-capacitor configuration.

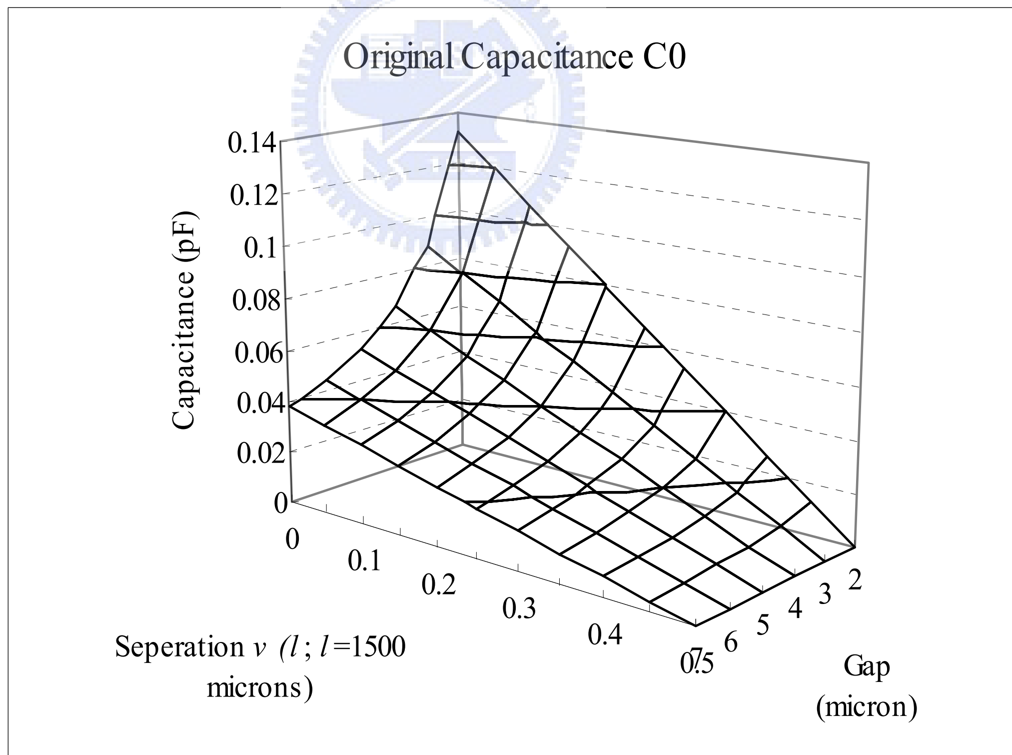

Figure 42 (b). The distribution of original capacitance Co when h=20 μ m.

Figure 42. The estimation of original capacitance Co.

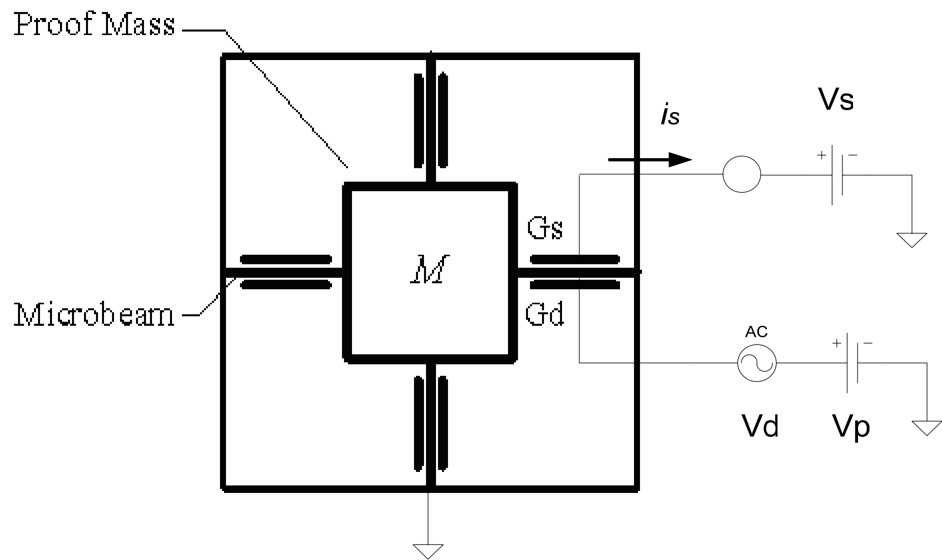

Figure 43 (a). Schematic diagram of driving and sensing circuit.

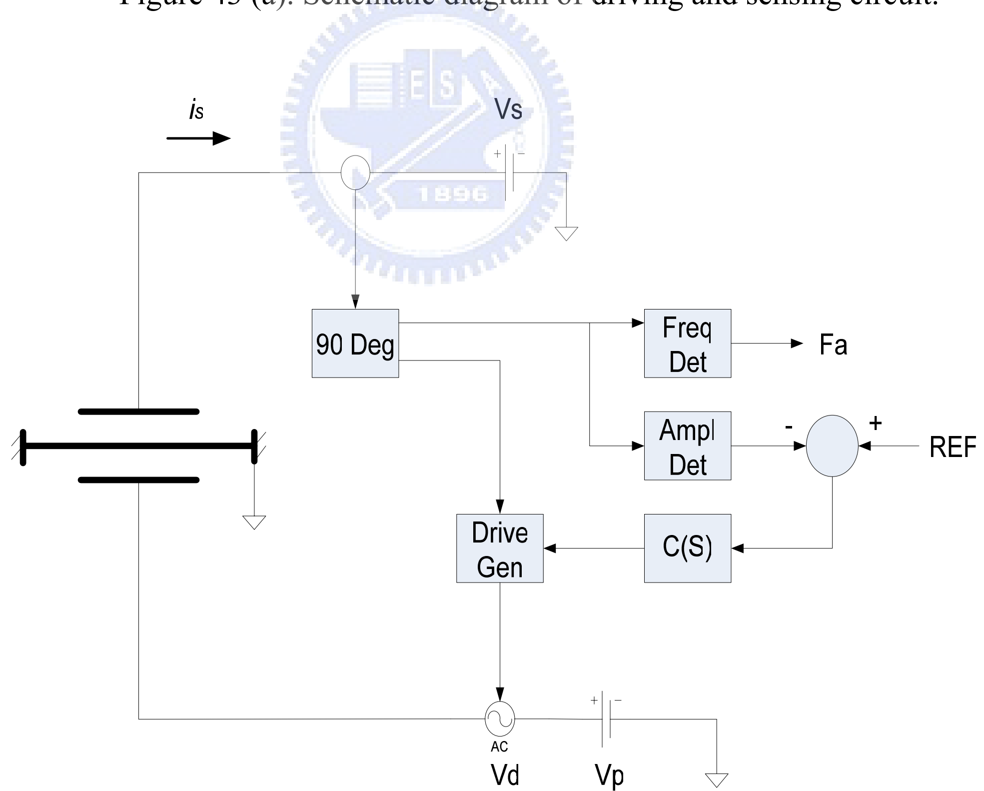

Figure 43 (b). Schematic diagram of PLL.

Figure 43. Schematic diagram of driving, sensing circuits and PLL.

Reference:

[1] Market analysis for Microsystems II, 2002-2005, A NEXUS Task Force Report, February, 2002.

[2] Stauffer Jean-Michel, "Market Opportunities for Advanced MEMS Accelerometer and Overview of Actual Capabilities vs. Required Specifications," PLANS 2004, Position Location & Navigation Symposium, IEEE.

[3] R. T. Howe and R. S. Muller, "Resonant-Microbridge Vapor Sensor," *IEEE Trans. Electron Devices*, vol. ED-33, pp. 499-506, April 1986.

[4] Trey A. Roger T. Howe, Albert P. Pisano, and James H. Smith, "Surface-Micromachined Resonant Accelerometer," Transducers '97, pp. 859-862, 1997 International Conference on Solid-State Sensors and Actuators, Chicago, 1997.

[5] S. C. Chang, M. W. Putty, D. B. Hicks and C. H. Li, "Resonant-bridge Two-axis Microaccelerometer," *Sensors and Actuators* A21-23, pp. 342-345, 1990.

[6] Yoshiteru Omura, Yutaka Nonomura and Osamu Tabata, "New Resonant Accelerometer Based on Rigidity Change," Transducers '97, pp. 855-858, 1997 International Conference on Solid-State Sensors and Actuators, Chicago, 1997.

[7] D. W. Burns, R. D. Horning, W. R. Herb, J. D. Zook and H. Guckel,"Sealed-cavity resonant microbeam accelerometer," *Sensors and Actuators* A53, pp. 249-255, 1996.

[8] H. Seidel, et al., "Capacitive Silicon Accelerometer with Highly Symmetrical Design," *Sensors and Actuators* A21-23, pp. 312~315, 1990.

[9] H. Lorenz, M. Despont, N. Fahrni, N. LaBianca, P. Renaud and P. Vettiger, "SU-8: a low cost negative resist for MEMS," *J. Micromech. Microeng.* Vol. 7,

pp. 121-124, 1977.

[10] Deng-Huei Hwang, Kanping Chin and Yi-Chung Lo, "On A Recipe For SU85 Photoresist To Fabricate The Electroplating Micromolds Of A Biaxial Microaccelerometer", *Proceeding of MST Conference* 2001, pp. 567-569.

[11] Deng-Huei Hwang, Kanping Chin and Yi-Chung Lo, "Modeling, Optimum Design and Fabrication for a Biaxial Frequency-Shifted Microaccelerometer", *Proceeding of MST Conference* 2001, pp. 297-302.

[12] A.A. Seshia, M. Palaniapan, et al., "A Vacuum Packaged Surface Micromachined Resonant Accelerometer," *Journal of Microelectromechanical Systems*, 11(6), 784-793 (2002).

[13] M. Ailele, K. Bauer, et al., "Resonant Accelerometer with Self-test," *Sensors and actuators* A 92, 161-167 (2001).

[14] R. Ohlckers, R. Holm, et al., "An integrated resonant accelerometer microsystem for automotive applications," *Sensors and Actuators* A 66, 99-104 (1998).

[15] Osamu Tabata and Rakeshi Yamamoto, "Two-axis detection resonant accelerometer based on rigidity change," *Sensors and Actuators* A 75, 53-59 (1999).

[16] S. Sung, J.G. Lee, et al., "Design and Performance Test of an Oscillation Loop for a MEMS Resonant Accelerometer," *Journal of Micromechanical and Microengineering* 13, 246-253 (2003).

[17] A.M. Hynes, H. Ashraf, J.K. Bhardwaj, J. Hopkins, I. Johnston, J.N. Shepherd, "Recent advances in silicon etching for MEMS using the ASE™ process," *Sensors and Actuators* A 74, 13-17 (1999).

[18] C. Burbaum, J. Mohr, and P. Bley, "Fabrication of Capacitive Acceleration Sensors by the LIGA Technique," *Sensors and Actuators* A 25-27, 559-563

(1991).

[19] H. Lorenz, M. Despnt, N. Fahrni, J. Brugger, P. Vettiger and P. Renaud, "High-aspect-ratio, ultrathick, negative-tone near-UV photoresist and its applications for MEMS," *Sensors and Actuators* A 64, 33-39 (1998).

[20] S. Andrew D. Dimarogonas and Sam Haddad, *Vibration For Engineer*, Prentice-Hall Inc, 1992.

[21] William T. Thomson, *Theory of Vibration with Application*, 3rd ed., Prentice-Hall Inc, 1988.

[22] F. P. Beer and E. R. Johnston, Jr., *Mechanics of Materials*, McGraw-Hill Ryerson Limited, 1987.

[23] LaBianca N. and Gelorme J. D., "High aspect Ratio Resist For Thick Film Applications," *SPIE* Vol. 2438, pp. 846-852, 1995.

[24] Despont et al, "High-Aspect-Ratio, Ultrathick, Negative-Tone Near-UV Photoresist For MEMS Applications", *Micro Electro Mechanical Systems. MEMS 98. Proceedings*, pp. 518-522, 1998.

[25] Dellmann et al, "Fabrication Process Of High Aspect Ratio Elastic Structures For Piezoelectric Motor Applications", *TRANSDUCERS '97*, pp. 641-644, 1997.

[26] Guérin et al, "Simple And Low Cost Fabrication Of Embeeded Micro-Channels By Using A New Thick-Film Photoplastic", *TRANSDUCERS '97*, pp. 1419-1422, 1997.

[27] Lorenz et al, "Mechanical Characterization of a New High-Aspect-Ratio Near UV-Photoresist", *Microelectronic Engineering* Vol. 41/42, pp. 371-374, 1998.

[28] Dellmann et al, "Fabrication process of high aspect ratio elastic and SU-8 structures for piezoelectric motor applications", *Sensors and Actuators*, A Vol. 70, pp. 42-47, 1998.

[29] Bertsch et al, "Combining Microstereolithography And Thick Resist UV Lithography For 3D Microfabrication", *Micro Electro Mechanical System, MEMS 98. Proceedings*, pp.18-23, 1998.

[30] David J. Elliott, Integrated Circuit Fabrication Technology, 2nd edition, McGRAW-Hill, 1989.

[31] Andojo Ongkodjojo and Francis E H Tay, "Global optimization and design for microelectromechanical systems devices based on simulated annealing," *Journal of Micromechanical and Microengineering* 12, 878–897 (2002).

[32] Dan Haronian, "Maximizing microelectromechanical sensor and actuator sensitivity by optimizing geometry," *Sensors and Actuators* A 50, 223-236 (1995).

[33] Ioan Pavelescuy, et al., "Analysis and modelling of a silicon micromachined Mach–Zehnder interferometer for pressure sensing," *Journal of Micromechanical and Microengineering* **7,** 214–217 (1997).

[34] S. P. Beeby and M. J. Tudor, "Modelling and optimization of micromachined silicon resonators," *Journal of Micromechanical and Microengineering* 5, 103-105 (1995).

[35] M. A. Meldrum, "Application of Vibrating Beam Technology to Digital Acceleration Measurement," *Sensors and Actuators* A 21-23, 377-380 (1990).

[36] R.P. van Kampen, R.F. Wloffenbuttel, "Modeling the mechanical behavior of bulk-micromachined silicon accelerometers," *Sensors and Actuators* A64, pp. 137-150, 1998.

Acknowledgements

This dissertation is dedicated to Prof. Kan-Ping Chin, who was the first author's adviser and initiated this research. Unfortunately, Dr. Chin passed away on February 8, 2002 (1960-2002) due to pneumonia.

Authors would like to thank Dr. S. C. Chang for his valuable suggestions on this research. Financial supports from the National Science Council of the Republic of China (Contract No. NSC88-2218-E-009-007) and the Materials Research and Development Center of CSIST (Contract No. BV89H14P) are acknowledged. The staffs at the Nano Facility Center of National Chiao Tung University are also appreciated for providing technical assistance.

Publication List

Journal Paper:

1. Deng-Huei Hwang, Kan-Ping Chin, Yi-Chung Lo and Wensyang Hsu, "Structure Design of A 2D High-Aspect-Ratio Resonant Microbeam Accelerometer", Journal of Microlithography, Microfabrication, and Microsystem. In press.

Conference Papers:

1. Deng-Huei Hwang, Kan-Ping Chin and Yi-Chung Lo, "Modeling, Optimum Design and Fabrication for a Biaxial Frequency-Shifted Microaccelerometer", Micro System Technologies 2001, Düsseldorf, March 27-29, 2001, International Conference & Exhibition on Micro Electro, Opto, Mechanical Systems and Components, pp. 290 ~ 302.
2. Deng-Huei Hwang, Kan-Ping Chin and Yi-Chung Lo, "On A Recipe For SU8-5 Photoresist to Fabricate The Electroplating Micromold of A Biaxial Microaccelerometer", Micro System Technologies 2001, Düsseldorf, March 27-29, 2001, International Conference & Exhibition on Micro Electro, Opto, Mechanical Systems and Components, pp. 567~569.
3. Deng-Huei Hwang, Yi-Chung Lo and Kan-Ping Chin, "Design considerations of the biaxial frequency-shifted microaccelerometer", Proceeding of SPIE, Design, Characterization, and Packaging for MEMS and Microelectronics II, Vol. 4593-15, pp. 62~71. SPIE Microelectronics and MEMS Conference, 17~19, December 2001, Adelaide, Australia.
4. Deng-Huei Hwang, Yi-Chung Lo and Kan-Ping Chin, "Development of a systematic recipe set for processing SU8-5 photoresist", Proceeding of SPIE, Device and Process Technologies for MEMS and Microelectronics II, Vol. 4592-14, pp. 131~139. SPIE Microelectronics and MEMS Conference, 17~19, December 2001, Adelaide, Australia.

Patent:

1. 中華民國發明專利證號：I220667, "液體噴射器製造方法(Method for manufacturing Liquid Injector)", 發明人：陳志明，黃鐙輝，陳昭晧，張永欣。專利核准日期：民國 93 年 9 月 1 日。

黃鐙輝之聯絡方式-

Email address:

lsy.hdh@msa.hinet.net; a1004@neostones.com.tw; frontier.me84g@nctu.edu.tw